2021

Accretion onto endoparasitic black holes at the center of neutron stars

Chloe B. Richards
Bowdoin College

Accretion onto endoparasitic black holes at the center of neutron stars

An Honors Paper for the Department of Physics and Astronomy

By Chloe B. Richards

Bowdoin College, 2021

Contents

Chapter 1

Introduction

1.1 Background

In this thesis we consider the accretion onto a non-rotating, endoparasitic[1] black hole residing at the center of a neutron star. We do so in order to extend previous work discussing the possibility of neutron stars as dark matter detectors (see e.g. Goldman and Nussinov (1989); de Lavallaz and Fairbairn (2010); Bramante and Linden (2014); Bramante and Elahi (2015); Capela et al. (2013); Bramante et al. (2018); East and Lehner (2019); Génolini et al. (2020)). We consider neutron stars to be possible dark matter detectors by supposing that they capture dark matter in the form of tiny black holes. Such systems evolve until the neutron star collapses, meaning the endoparasitic black hole residing at the center will accrete all matter from the neutron star. Currently, one constraint on black holes as sources of dark matter arises from the existence of neutron star populations.

The scenario above can be considered in at least two different ways, namely the neutron star captures a primordial black hole (PBH) or some other dark matter particles. In the former case, we consider the possibility that PBHs, which formed in the early universe (see Hawking (1971); Carr and Hawking (1974)) can be captured by neutron

[1] We define endoparasitic to describe a tiny body residing inside a much larger body

stars. After capture, the PBH resides at the center of the neutron star and accretes matter until the star completely collapses (see Hawking (1971); Markovic (1995)). In the latter case, we consider that dark matter particles captured by a neutron star may under favorable conditions, collapse to form a small black hole (see Goldman and Nussinov (1989); de Lavallaz and Fairbairn (2010); Bramante and Linden (2014); Bramante et al. (2018)).

After the black hole has been either captured by the neutron star or forms inside the neutron star, the resulting system evolves until the black hole completely consumes the neutron star. A number of authors including Fuller et al. (2017); Takhistov et al. (2020); Génolini et al. (2020) have discussed observational signatures of such a process. Numerical simulations by East and Lehner (2019) consider three different equations of state for both rotating and non-rotating neutron stars. Their simulations were restricted to relatively large black hole masses $M_{\rm BH}/M \geq 10^{-2}$, where M is the neutron star mass. Through their simulations, they determined that the accretion rate follows the relation $\dot{M}_{\rm BH} \propto M_{\rm BH}^2$ as suggested by Bondi (see Bondi (1952); see Shapiro and Teukolsky (2004) for a textbook treatment). Furthermore, their results concluded that the accretion rate was largely independent of the neutron star spin, which agrees with results from Kouvaris and Tinyakov (2014).

1.2 Summary

We extend previous work on the accretion process of tiny black holes residing at the center of neutron stars in several ways in this thesis. Bondi accretion for an isolated black hole, i.e. where the gravitational forces are dominated by the black hole, is well understood. To determine the Bondi accretion rate for our system, we consider a space-time describing a black hole in the interior of a neutron star. Additionally, we determine such Bondi accretion for stiff equations of state. In Chapter 2, we give a general treatment

of Bondi accretion as described by Bondi (1952); Shapiro and Teukolsky (2004). For stiff equations of state with $\Gamma > 5/3$, we find the accretion rate under a relativistic treatment (see Appendix G in Shapiro and Teukolsky (2004)) and identify an associated minimum accretion rate. We do so in order to determine the accretion rate for our neutron star system described by a stiff, polytropic equation of state with adiabatic index $\Gamma = 2$.

In Chapter 3, we then adopt our relativistic Bondi accretion model to describe a non-rotating black hole residing at the center of a neutron star. We crudely integrate the resulting equations both including and ignoring stellar evolution in order to give estimates for the lifetime of our neutron star model.

In Chapter 4 we perform numerical simulations in full general relativity, extending previous results of East and Lehner (2019). We focus on spherical neutron stars with non-rotating black holes at the center. Our system adopts a stiff, polytropic equation of state with adiabatic index $\Gamma = 2$, which is commonly used to describe neutron stars in numerical simulations. We implement our code using spherical polar coordinates (see Baumgarte et al. (2013, 2015)) and a logarithmic radial coordinate in order to resolve the vastly different length scales between the black hole mass and the neutron star mass. We extend the work of East and Lehner (2019) by considering black holes with mass ratios as small as $M_{\rm BH}/M \simeq 10^{-9}$. With such small masses, we extend into the mass range of PBHs and black hole dark matter candidates. Our mass range gives black hole masses comparable to that of dwarf planets.

We compare our analytical estimates with our numerical results in Chapter 5. We find excellent agreement between our analytical Bondi flow and the numerical rest-mass flux. For larger black hole masses, we evolve the system until the neutron star is completely consumed and compare with our analytical results accounting for and ignoring stellar evolution. We present both our analytical Bondi accretion rates and our numerical accretion rates in Table 5.1.

We summarize our findings for a large range of black hole masses in Fig. 1.1 for

both our analytical estimates and numerical results. In Fig. 1.1, the solid line represents the analytical accretion rate for our fiducial neutron star model from Eq. (3.42), and the dashed line represents the corresponding minimum accretion rate given by Eq. (3.43). We note that such a minimum accretion rate exists only for stiff equations of state with $\Gamma > 5/3$. Our numerical results are presented through two different measurements of the accretion shown as triangles and open circles. The triangles represent the growth of the black hole mass with respect to time. As shown in the Figure, we are only able to compute this accretion for "large" black hole masses because the accretion rate is proportional to the square of the black hole mass, so the accretion rate becomes exceedingly small and difficult to determine numerically from the growth of the black hole. We are able to compute the accretion rate by measuring rest-mass flux across the horizon of the black hole for all black hole masses as shown by the open circles and find excellent agreement with our analytical estimates. Furthermore, we confirm that Bondi accretion for a stiff equation of state accurately describes the accretion onto an endoparasitic black hole at the center of our neutron star model, and therefore, we are able to use these analytical expressions to determine the lifetimes of such neutron stars.

Throughout this thesis we use geometrized units with $G = 1 = c$ unless noted otherwise where G is the gravitational constant and c is the speed of light.

1.3 Contributions

This thesis is based on collaborative work that resulted in the two publications Richards et al. (2021b) and Richards et al. (2021a). I would like to highlight my primary contributions:

- Derived the Bondi accretion for stiff equations of state in Section 2.1
- Determined data describing our fiducial neutron star model presented in Table 3.2
- Performed all numerical solutions described in Chapter 4

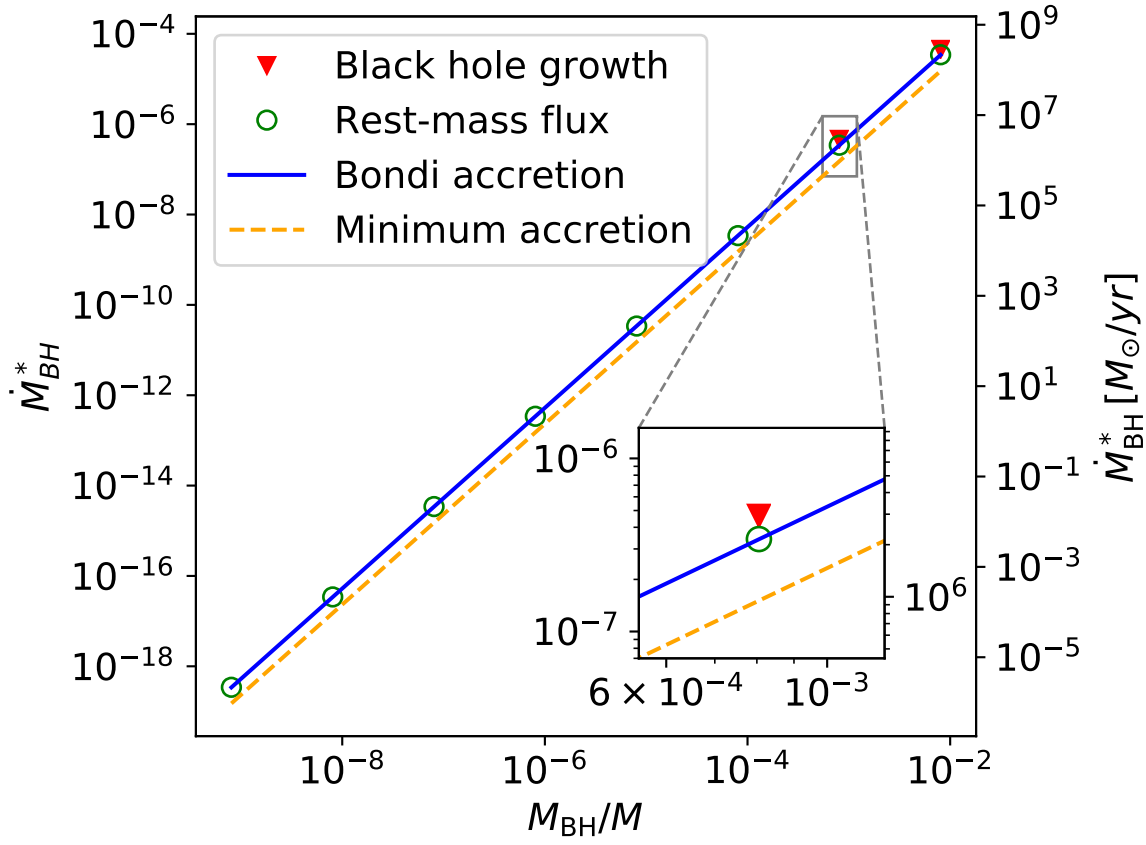

Figure 1.1: Comparison of analytical and numerical accretion rates $\dot{M}^\star_{\rm BH}$ for various black holes with initial mass $M_{\rm BH}(0)$ for our fiducial neutron star model with $\Gamma = 2$. We express the accretion rate in geometrized units on the right-hand side of the plot and we express it in units of solar masses per year on the left-hand side. The solid blue line represents the analytical Bondi accretion rate given by Eq. (3.42). The numerical results for the accretion rate are shown by red triangles and open green circles, representing the growth of the black hole mass and the rest-mass flux over the black hole horizon respectively. The dashed orange line represents the minimum accretion rate for a $\Gamma = 2$ polytrope as given by (3.43). (See also Table 5.1 for a detailed listing of these results.) In the inset, we show the all numerical and anayltical results for one particular black hole $M_{\rm BH}/M \simeq 10^{-3}$. we notice the excellent agreement between the analytical Bondi accretion for stiff equations of state and numerical rest-mass flux. The numerical accretion given by black hole growth differs slightly from the analytical estimate as it includes thermal energy in addition to rest-mass.

- Determined numerical data for our numerical simulations presented in Table 5.1

Chapter 2

Bondi accretion

We use Bondi accretion to consider our model of a black hole embedded in a neutron star. Newtonian Bondi accretion as outlined in Bondi (1952) describes the steady-state, spherically symmetric flow of gas onto a point mass. We assume the gas to be governed by a polytropic equation of state $P = K\rho_0^\Gamma$, where K is a constant and Γ is the adiabatic index. In this chapter, we will a derive a general solution for all adiabatic indices in the range $1 < \Gamma < 3$. We note that the Newtonian treatment breaks down for $\Gamma > 5/3$ so that we need to employ a relativistic treatment. Furthermore, we will specify our result for $\Gamma = 2$, which is an adequate approximation for the equation of state of a neutron star and therefore allows us to consider accretion onto a black hole at the center of a neutron star.

2.1 General treatment

To consider relativistic spherical Bondi flow onto an endoparisitic black hole, we follow Michel (1972) to ignore the inflow's self-gravity. Rather than adopting the Schwarzschild metric in its usual form,

$$ds^2 = -\left(1 - \frac{2M}{r}\right) dt^2 + \left(1 - \frac{2M}{r}\right)^{-1} dr^2 + r^2 d\Omega^2, \tag{2.1}$$

to describe the geometry of spacetime, we will allow for the general form

$$ds^2 = -\left(e^{2D} - \frac{\kappa}{R}\right) dt^2 + \left(1 - \frac{e^{-2D}\kappa}{R}\right)^{-1} dR^2 + R^2 d\Omega^2. \tag{2.2}$$

In the above, M is the mass of our black hole and D and κ are constants of integration.

As described in Appendix A in Richards et al. (2021a), we adopt the generalized Schwarzschild metric given by (2.2) to re-derive the Bondi accretion equations for a black hole at the center of a neutron star. We define a local asymptotic observer to be one who is far from the black hole, but well within the radius of the neutron star. For the purposes of this chapter, a local asymptotic observer is identical to an asymptotic observer at infinity because we are considering an isolated black hole, i.e. without a neutron star. The local asymptotic observer becomes important, however, in Chapter 3 as we then consider a black hole inside a neutron star. We note that we recover the Schwarzschild metric (2.1) for $D = 0$ and $\kappa = 2M$.

Now we consider the accretion rate $\dot{M}$ at the critical radius r_s as described by hydrodynamic spherical accretion in Eq. (14.3.4) of Shapiro and Teukolsky (2004),

$$\dot{M} = 4\pi\rho_{0s} u_s r_s^2, \tag{2.3}$$

where ρ_0 is the rest mass density and u describes the radial component of the fluid 4-velocity $u \equiv -u^r$. Here, the critical radius r_s reduces to the transonic point in a Newtonian limit. In the relativistic limit, we assume that the flow is subsonic asymptotically and therefore must past through the critical radius r_s (see Appendix G in Shapiro and Teukolsky (2004)). For the remainder of this thesis, any variable with the subscript s is evaluated at the critical radius r_s. Furthermore, when referencing the asymptotic region where $r \to \infty$, variables will be marked with a subscript ∞ (for example, a_∞ is the asymptotic sound speed).

To avoid singularities in $\dot{M}$, we define the critical flow velocity u_s as

$$u_s = \frac{a_s}{a_\infty}\left(1 + 3a_s^2\right)^{-1/2} a_\infty \tag{2.4}$$

and critical radius r_s as

$$r_s = \frac{a_\infty^2}{a_s^2}\frac{1 + 3a_s^2}{2}\frac{M}{a_\infty^2} \tag{2.5}$$

as shown in Eq. (G.17) of Shapiro and Teukolsky (2004). Here we define the sound speed a in terms of pressure P and density ρ

$$a^2 = \left.\frac{dP}{d\rho}\right|_s = \left.\frac{dP}{d\rho_0}\right|_s \frac{\rho_0}{\rho + P}, \tag{2.6}$$

where derivatives are taken at constant entropy. We assume a polytropic equation of state

$$P = K\rho_0^\Gamma, \tag{2.7}$$

where K is a constant and Γ the adiabatic index. The adiabatic index Γ parameterizes the stiffness of the equation. For $\Gamma \geq 5/3$, increasing density ρ_0 results in an increased pressure P, so for the purposes of this discussion, we will refer to all $\Gamma \geq 5/3$ as describing stiff equations of state. The sound speed is related to rest-mass density ρ_0 by

$$a^2 = \frac{\Gamma K \rho_0^{\Gamma-1}}{1 + \Gamma K \rho_0^{\Gamma-1}/(\Gamma - 1)}. \tag{2.8}$$

We notice that for finite densities ρ_0, the sound speed must be smaller than a maximum value $a_{\max}$,

$$a^2 < a_{\max}^2 = \Gamma - 1. \tag{2.9}$$

We evaluate Eq. (2.8) at the critical radius r_s and in the asymptotic region where $r \to \infty$ to find a relationship between the rest-mass density ρ_{0s} and the rest-mass density's

asymptotic value $\rho_{0\infty}$,

$$\rho_{0s} = \left(\frac{a_s}{a_\infty}\right)^{2/(\Gamma-1)} \left(\frac{\Gamma - 1 - a_\infty^2}{\Gamma - 1 - a_s^2}\right)^{1/(\Gamma-1)} \rho_{0\infty}. \tag{2.10}$$

Inserting (2.4), (2.5), and (2.10) into (2.3) we now find

$$\dot{M} = 4\pi\lambda_{\rm GR} \left(\frac{M}{a_\infty^2}\right)^2 \rho_{0\infty} a_\infty, \tag{2.11}$$

where

$$\lambda_{\rm GR} \equiv \left(\frac{a_s}{a_\infty}\right)^{(5-3\Gamma)/(\Gamma-1)} \left(\frac{\Gamma - 1 - a_\infty^2}{\Gamma - 1 - a_s^2}\right)^{1/(\Gamma-1)} \frac{(1+3a_s^2)^{3/2}}{4} \tag{2.12}$$

is a dimensionless "accretion rate eigenvalue".

We note that the relationship between the sound speeds a_s and a_∞ in the second term of (2.12) dictates the limiting value of $_{\rm GR}$ as $a_\infty \to 0$. For soft equations of state, $\lambda_{\rm GR}$ reaches a non-zero value as $a_\infty \to 0$ as shown in Figure (2.1). However, for stiff equations of state, $\lambda_{\rm GR} \to 0$ as $a_\infty \to 0$ in order to maintain a finite accretion rate as given by (2.11).

While $\lambda_{\rm GR}$ describes the accretion rate eigenvalue in general for all solutions, we can simplify it by considering it in the Newtonian limit, where $a_s \ll 1$ and $a_\infty \ll 1$, meaning the sound speed in both the inner and outer asymptotic regions are significantly smaller than the speed of light $c = 1$. Under this treatment, Eq. (2.12) reduces to the Newtonian accretion eigenvalue λ_s,

$$\lambda_s = \frac{1}{4}\left(\frac{a_s}{a_\infty}\right)^{(5-3\Gamma)/(\Gamma-1)}. \qquad \text{(Newtonian)} \tag{2.13}$$

From Shapiro and Teukolsky (2004) (14.3.14), we also have

$$\frac{a_s}{a_\infty} = \left(\frac{2}{5-3\Gamma}\right)^{1/2} \qquad \text{(Newtonian)} \tag{2.14}$$

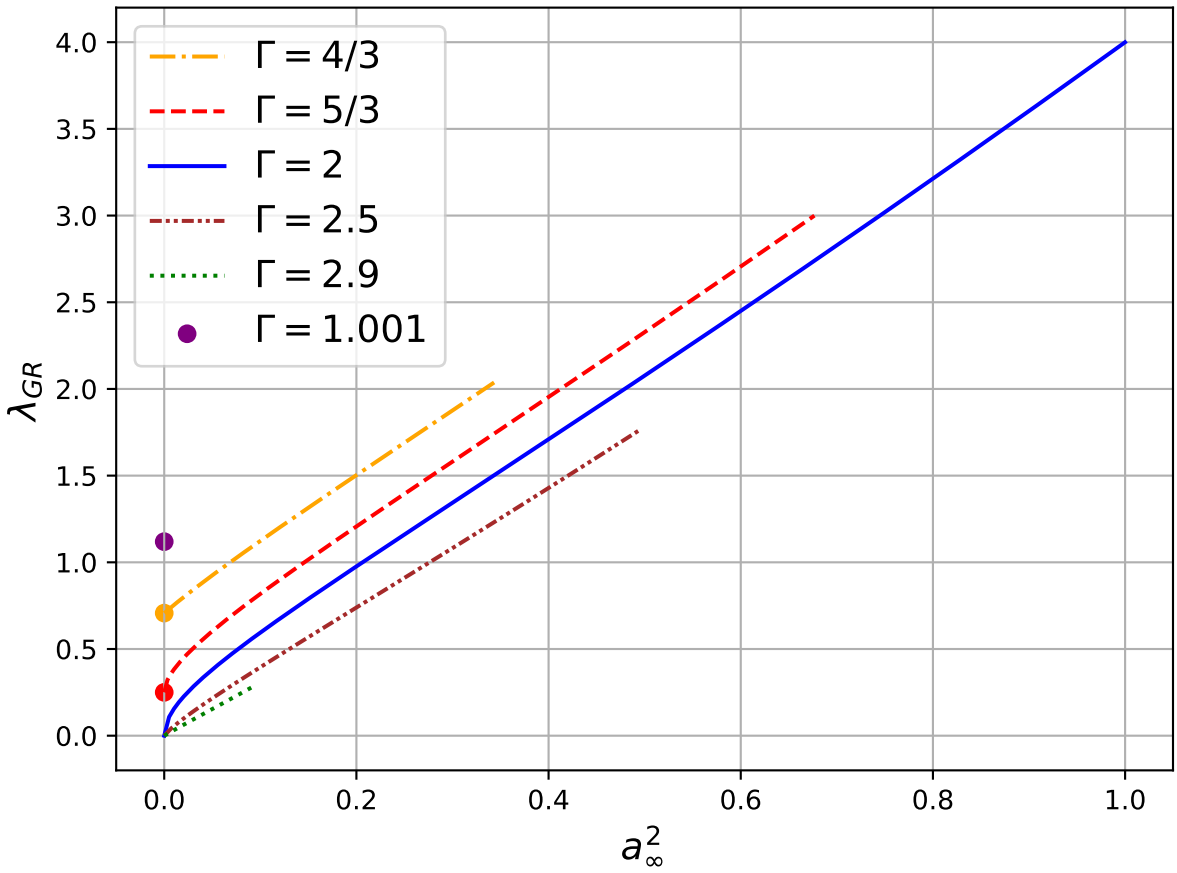

Figure 2.1: Solutions for accretion rate eigenvalue $\lambda_{\rm GR}$ as given by Eq. (2.12) for various values of Γ, as a function of a_∞^2. Although we focus on stiff equations of state, we include λ_{GR} for $\Gamma < 5/3$ to show the discontinuity in accretion eigenvalues in the Newtonian limit $a_\infty^2 \ll 1$. For soft equations of state $\Gamma < 5/3$ the accretion eigenvalues $\lambda_{\rm GR}$ approach the Newtonian values λ_s shown by the dots (see Eq. (2.15) as $a_\infty \to 0$), whereas for $\Gamma \geq 5/3$ λ_{GR} approaches zero in that limit. This result for stiff equations of state is necessary in order to maintain a finite accretion rate $\dot{M}$ when considering stiff equations of state $\Gamma \geq 5/3$ in the limit of low asymptotic sound speed $a_\infty^2 \ll 1$.

in the Newtonian limit, which we can insert into (2.13) to obtain the Newtonian accretion eigenvalues

$$\lambda_s = \frac{1}{4}\left(\frac{2}{5-3\Gamma}\right)^{(5-3\Gamma)/2(\Gamma-1)}, \qquad \text{(Newtonian)} \tag{2.15}$$

which are given by dots in Figure (2.1). We confirm this result for the Newtonian accretion eigenvalues with Eq. (14.3.17) and Table 14.1 from Shapiro and Teukolsky (2004). As we can see, the Newtonian treatment breaks down for adiabatic indices $\Gamma > 5/3$. We note that the Newtonian accretion eigenvalues λ_s depend on only Γ, while the relativistic accretion eigenvalues $\lambda_{\rm GR}$ also depend on the critical and asymptotic sound speeds a_s and a_∞ respectively. Therefore, we require a relativistic treatment for stiff equations of state with $\Gamma > 5/3$ which we will describe in the following.

To solve for our accretion rate $\dot{M}$ we consider the relationship between the sound speeds in the inner and outer asymptotic regions

$$(1+3a_s^2)\left(1-\frac{a_s^2}{\Gamma-1}\right)^2 = \left(1-\frac{a_\infty^2}{\Gamma-1}\right)^2 \tag{2.16}$$

as shown in Eq. (G.30) in Shapiro and Teukolsky (2004), which we now write as a cubic equation for a_s^2

$$a_s^6 + \frac{a_s^4}{3}(7-6\Gamma) + \frac{a_s^2}{3}(3\Gamma^2-8\Gamma+5) + \frac{a_\infty^2}{3}(2\Gamma-2-a_\infty^2) = 0, \tag{2.17}$$

We write this equation in the form

$$x^3 + Ax^2 + Bx + C = 0 \tag{2.18}$$

for $x = a_s^2$ and identify the coefficients

$$\begin{aligned} A &= \frac{1}{3}(7 - 6\Gamma) \\ B &= \frac{1}{3}(1 - \Gamma)(5 - 3\Gamma) \\ C &= \frac{a_\infty^2}{3}(2\Gamma - 2 - a_\infty^2), \end{aligned} \tag{2.19}$$

noting that all three coefficients A, B, and C are real.

We solve the cubic equation (2.18) in detail in Appendix A and find that while there are three solutions $x_1, x_2,$ and x_3 given by (A.5), only x_3 gives a physically viable solution.

As an aside, we note that we can also rewrite Eq. (2.16) as a quadratic equation for a_∞^2

$$a_\infty^2 = \Gamma - 1 \pm \left\{(\Gamma - 1)^2 + 3\left(a_s^6 + A a_s^4 + B a_s^2\right)\right\}^{1/2}. \tag{2.20}$$

For most applications, however, we consider a_∞ as given and therefore solve the cubic equations (2.18) for a_s.

As mentioned above, Eq. (2.9) gives a condition for determining all physical solutions for $\Gamma \leq 2$. However, we must impose causality explicitly for $\Gamma > 2$ to find all physical solutions, and we find that this condition holds only for sufficiently small a_∞. Since for these solutions we find that $a_s > a_\infty$, we plug $\Gamma = 2$ into Eq. (2.9) and insert the result $a_{s,max} = 1$ into Eq. (2.20) to find

$$a_{\infty,max}^2 = 3 - \Gamma \tag{2.21}$$

where we have picked the "-" solution in Eq. (2.20) since the "+" solution, $3\Gamma - 5$, is not relevant for $\Gamma > 2$. This upper limit for the sound speed in the asymptotic region a_∞ holds for $\Gamma > 2$. However, a_∞ must be positive, so we note that physical solutions are non-existent for $\Gamma \geq 3$.

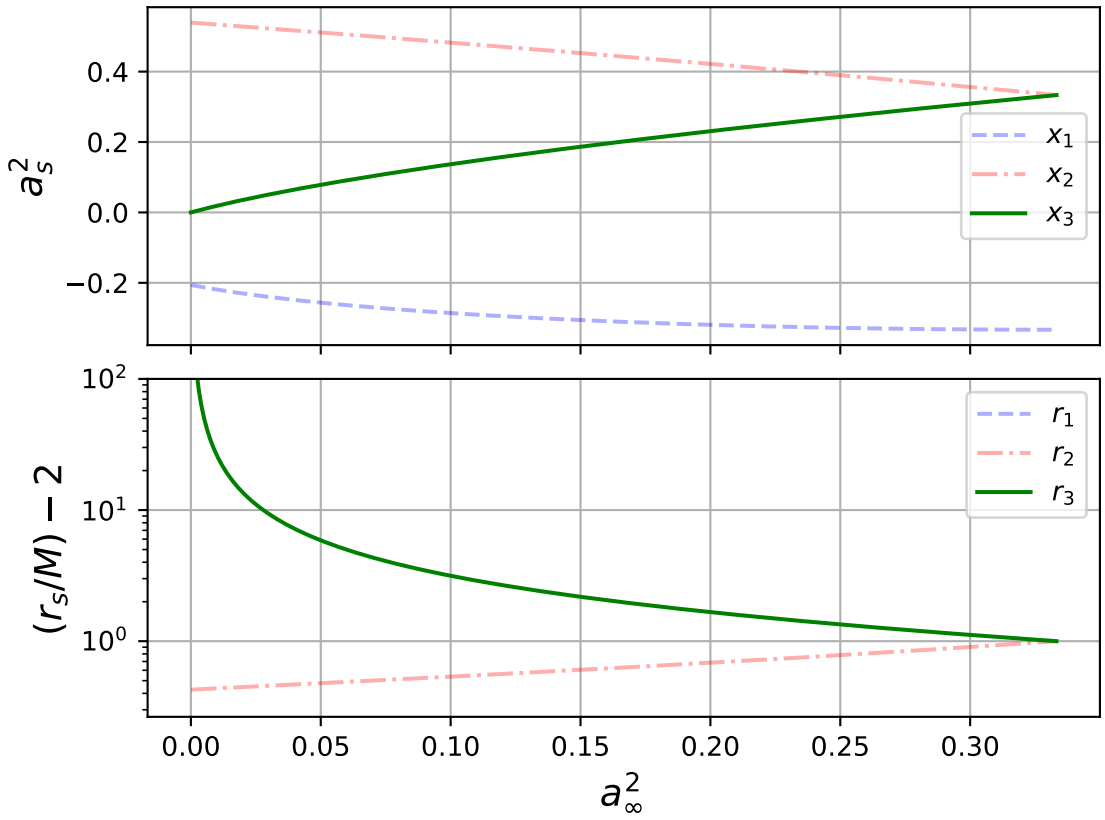

Figure 2.2: Top panel: Three real roots x_1, x_2, x_3 to the cubic equation Eq. (2.18) for $\Gamma = 4/3$, as a function of a_∞^2. We note that the thick green line x_3 is the only physical solution. $x_1 < 0$ gives an unphysical solution ($a_s^2 < 0$) and x_2 gives a wind, or outgoing, solution as inserting a_s into (2.4) would yield $u < 0$, i.e. $u^r > 0$. Lower panel: The critical radius associated with the roots in the top panel.

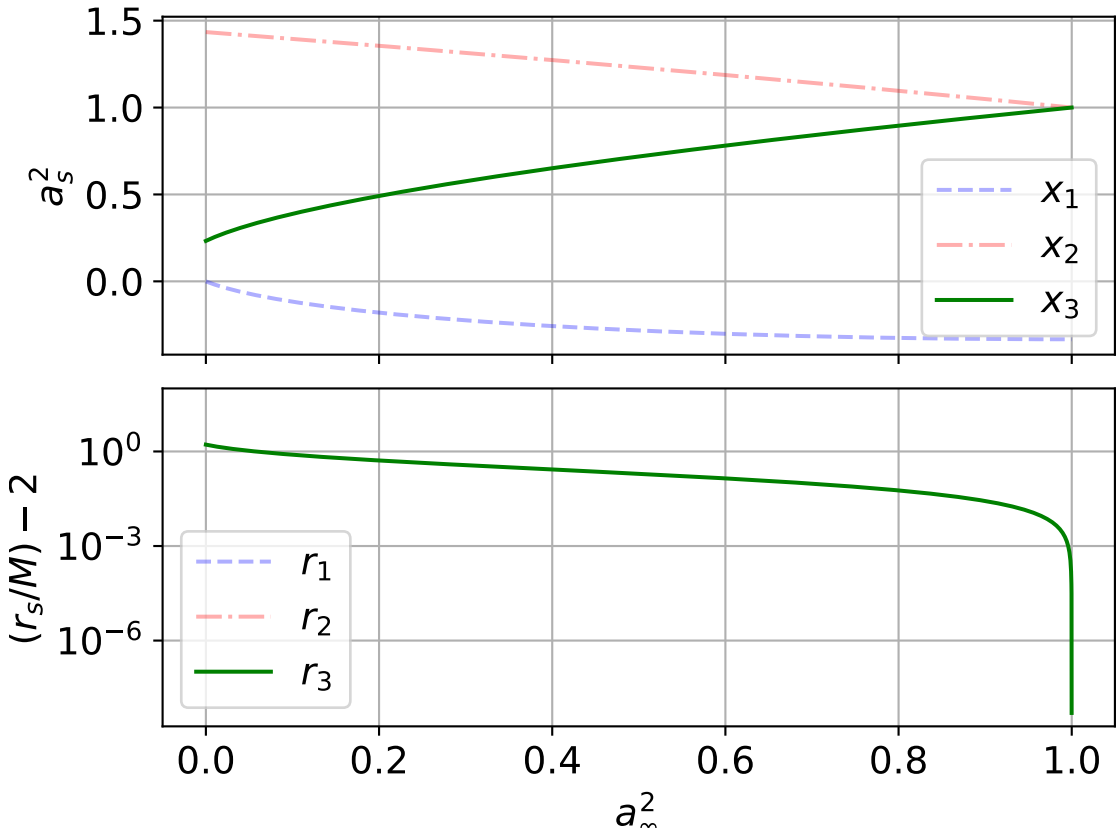

Figure 2.3: Same as Figure (2.2), but for $\Gamma = 2$ as a model for accretion onto a black hole at the center of a neutron star. Different from Fig. (2.2) however, we note that the physical solution x_3 for a_s^2 has a nonzero value as $a_\infty^2 \to 0$, as shown by Eq. (2.27).

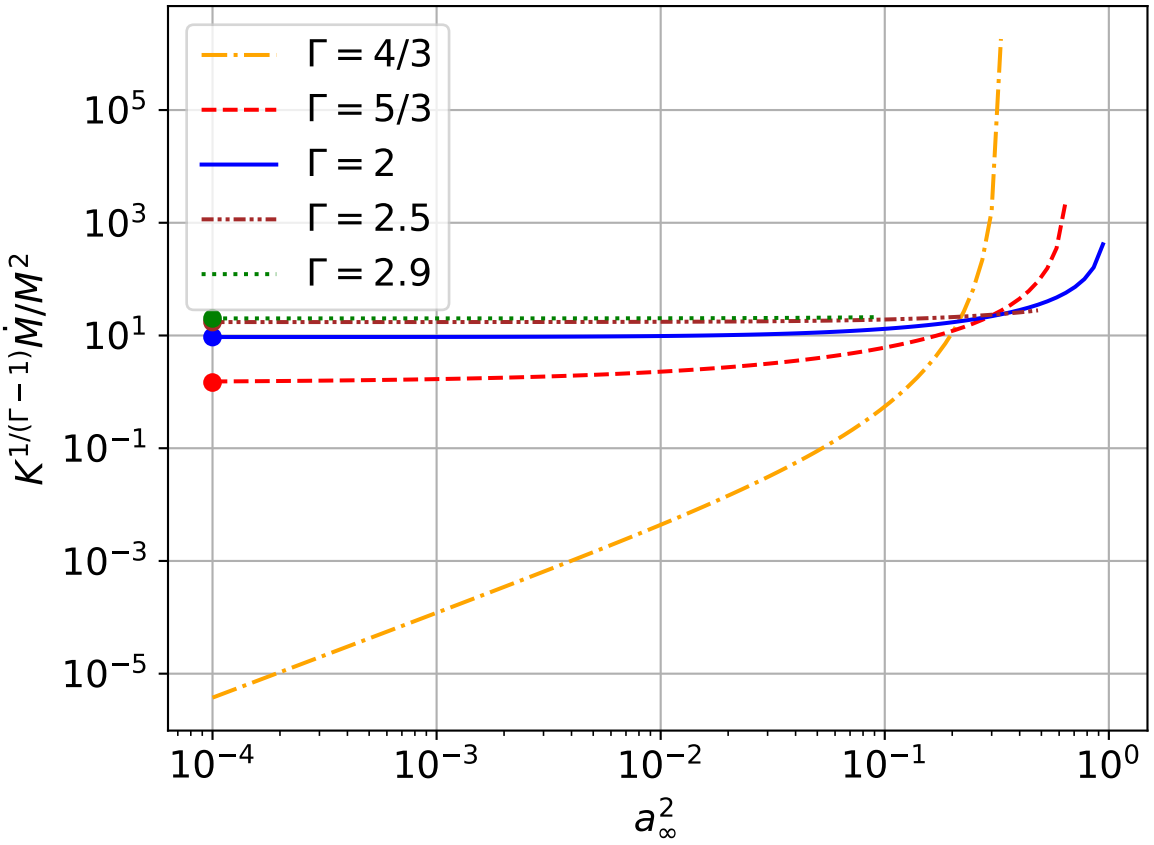

Figure 2.4: Accretion rate $\dot{M}$ as scaled by the black hole mass M and polytropic constant K for various values of adiabatic index Γ. For $\Gamma < 5/3$ these accretion rates approach zero as $a_\infty^2 \to 0$, but for stiff equations of state with $\Gamma \geq 5/3$ they approach a finite, non-zero value. We include the minimum accretion rates given by Eq. (2.32) as the dots.

2.2 Minimum accretion

We reference Begelman (1978) to begin with the limit of low asymptotic sound speeds $a_\infty^2 \ll 1$. In this limit, the rest-mass density can be approximated from (2.8),

$$\rho_0 = \left(\frac{a^2}{\Gamma K}\right)^{1/(\Gamma-1)} \left(1 + \mathcal{O}(a^2)\right) \qquad (a^2 \ll 1) \tag{2.22}$$

and we may express the accretion rate (2.11) as

$$\dot{M} = 4\pi\lambda_{\rm GR} \frac{M^2}{(\Gamma K)^{1/(\Gamma-1)}} a_\infty^{(5-3\Gamma)/(\Gamma-1)} \left(1 + \mathcal{O}(a_\infty^2)\right) \qquad (a_\infty^2 \ll 1) \tag{2.23}$$

When considering $a_\infty = 0$, we note that the coefficient C vanishes in Eq. (2.19), so the solutions to the cubic equation (2.18) are given by

$$\begin{aligned} \bar{x}_1 &= 0 \\ \bar{x}_2 &= \Gamma - 7/6 + (12\Gamma - 11)^{1/2}/6 \qquad (a_\infty^2 = 0) \\ \bar{x}_3 &= \Gamma - 7/6 - (12\Gamma - 11)^{1/2}/6. \end{aligned} \tag{2.24}$$

As we demonstrate below, when considering stiff equations of state, each of the solutions is associated with the respective root from (A.5).[1]

Now, we rewrite the roots to the cubic equation to leading order in a_∞^2,

$$\begin{aligned} x_1 &= a_1\, a_\infty^2 \\ x_2 &= \bar{x}_2 + a_2\, a_\infty^2 \qquad (a_\infty^2 \ll 1) \\ x_3 &= \bar{x}_3 + a_3\, a_\infty^2. \end{aligned} \tag{2.25}$$

[1] We note that this equation can be written in a more general notation with Roman numeral subscripts as seen in Eq. (33) in Richards et al. (2021b) because Γ determines which of the roots above should be identified with the three roots from (A.5). For soft equations of state $\Gamma \leq 5/3$, we identify x_I with our solution x_3 from (A.5). For our case, however, we only consider stiff equations of state $\Gamma > 5/3$ which identifies x_{III} with our solution x_3. Therefore, we feel comfortable adopting this more specified notation.

where the coefficients a_1, a_2, and a_3 are given by

$$\begin{aligned} a_1 &= \frac{2}{5-3\Gamma} \\ a_2 &= -\frac{2}{5-3\Gamma}\,\frac{\bar{x}_2+A}{\bar{x}_2-\bar{x}_3} \\ a_3 &= \frac{2}{5-3\Gamma}\,\frac{\bar{x}_3+A}{\bar{x}_2-\bar{x}_3}. \end{aligned} \tag{2.26}$$

Looking closely, we observe that B, $\bar{x}_3$, the coefficients (2.26), and the exponent of the first term in (2.12) all change sign at $\Gamma = 5/3$. The coefficients (2.26) diverge for $\Gamma = 5/3$, meaning that the expansion does not converge in this case, and that we have to treat the cases $\Gamma \leq 5/3$ and $\Gamma > 5/3$ separately. Since $\Gamma = 2$ gives the solution for our neutron star model, we will consider the case for stiff equations of state $\Gamma > 5/3$. (For a full treatment, see Richards et al. (2021b)).

For the rest of the chapter, we will be considering stiff equations of state $\Gamma > 5/3$. First, we note that the coefficient $a_1 < 0$, meaning x_1 in (2.25) is not a physical solution. Similarly, $x_2 > 1$ gives an outgoing solution, meaning solutions describing wind rather than accretion, for all $\Gamma > 5/3$. Hence, we identify our solution to be $a_s^2 = x_3$, i.e.

$$a_s^2 = \bar{x}_3 + a_3\, a_\infty^2 + \mathcal{O}(a_\infty^4). \tag{2.27}$$

From Fig. (2.3), we see that a_s^2 takes a non-zero value as $a_\infty^2 \to 0$. This result tells us that for smaller values of a_s, the solution is local rather than global as it cannot extend to infinity (see Chaverra et al. (2016)). Furthermore, we note that $a_s^2 \geq 1$ for $\Gamma \geq 3$, so we restrict our focus to the physical regime $5/3 < \Gamma < 3$.

To find our accretion rate under the low asymptotic sound speed limit, insert (2.27) into (2.5)

$$r_s = \frac{M}{2\bar{x}_3} = \frac{M}{2\Gamma - 7/3 - (12\Gamma-11)^{1/2}/3}, \qquad (a_\infty^2 \ll 1,\ \Gamma > 5/3) \tag{2.28}$$

showing it is independent of a_∞^2 to leading order. Now we can rewrite the accretion eigenvalues from Eq. (2.12) by noticing that the first term becomes

$$\frac{a_\infty}{a_s} = \bar{x}_3^{-1/2} a_\infty + \mathcal{O}(a_\infty^3), \tag{2.29}$$

giving the accretion eigenvalues for our solution

$$\lambda_{GR} = \bar{\lambda}\, a_\infty^{(3\Gamma-5)/(\Gamma-1)} \left(1 + \mathcal{O}(a_\infty^2)\right) \qquad (\Gamma > 5/3) \tag{2.30}$$

with

$$\bar{\lambda} = \bar{x}_3^{(5-3\Gamma)/(2(\Gamma-1))} \left(\frac{\Gamma - 1}{\Gamma - 1 - \bar{x}_3}\right)^{1/(\Gamma-1)} \frac{(1 + 3\bar{x}_3)^{3/2}}{4}. \tag{2.31}$$

The accretion eigenvalues (2.30) vanish in the limit of $a_\infty^2 \to 0$. Although we did not give a treatment for soft equations of state $\Gamma \leq 5/3$, we note that $\lambda_{\rm GR}$ does not vanish in the limit of $a_\infty^2 \to 0$ as seen in Fig. (2.1). Now we insert our accretion eigenvalue (2.30) into the accretion rate (2.11) to obtain

$$\dot{M} = 4\pi\bar{\lambda}\, \frac{M^2}{(\Gamma K)^{1/(\Gamma-1)}}. \qquad (a_\infty^2 \ll 1,\ \Gamma \geq 5/3) \tag{2.32}$$

At this point, we take a moment to recognize and appreciate that under the limit where the sound speed and rest-mass density go to zero, the accretion rate (2.32) takes a non-zero value. Therefore, we conclude these limiting values give a minimum for stiff equations of state $\Gamma > 5/3$ as demonstrated in Fig. (2.4) where the dots represent the given minima for each Γ. The minimum accretion rate given by Eq. (2.32) depends on M, Γ, and K, where the latter two variables are determined by the chosen equation of state. For our purposes we wish to find our solution for a neutron star with $\Gamma = 2$ which gives

$$\bar{\lambda} \simeq 1.49 \qquad (\Gamma = 2) \tag{2.33}$$

and

$$\dot{M}_{\min} \simeq 9.39 \frac{M^2}{K}. \qquad (\Gamma = 2) \tag{2.34}$$

To further specify our solution, we identify our value of K which is determined by our chosen equation of state and physical values for our neutron star model as outlined in Section 3.4.

Chapter 3

Analytical Estimates of accretion rates and accretion times

This chapter presents the analytical results derived for the accretion rate and lifetime of our black hole. In Section 3.4 of this chapter, we describe our fiducial neutron star model which captures our black hole. We adopt this fiducial neutron star model for all of our numerical simulations described in Chapter 4.

3.1 Accretion rates

To begin our analytical estimates, we assume that a non-spinning black hole with mass $M_{\rm BH}$ is at the center of a spherically symmetric neutron star with $M > M_{\rm BH}$ and radius $R \gg M_{\rm BH}$. Without the presence of the black hole, the neutron star is in hydrostatic equilibrium. Therefore, matter is at rest far from the black hole where the black hole resides in a nearly homogeneous core. To begin estimating the rate at which the black hole accretes matter from the neutron star, we define the capture radius

$$r_a \equiv M_{\rm BH}/a_c^2, \tag{3.1}$$

which describes the radius at which the internal energy, $\frac{1}{2}ma^2$, is equal to the gravitational energy, $mM_{\rm BH}/r$, to order of magnitude. Here a_c describes the sound speed evaluated at the center of the unperturbed star. Recall that the sound speed is given by (2.6),

$$a^2 = \left.\frac{dP}{d\rho}\right|_s = \left.\frac{dP}{d\rho_0}\right|_s \frac{\rho_0}{\rho + P}, \tag{3.2}$$

where P is the pressure, ρ is the total mass-energy density, ρ_0 is the rest-mass density, and we take the derivative at constant entropy. In the Newtonian treatment in this section, we do not need to distinguish between ρ and ρ_0, but we introduce them here for later reference. As mentioned in Chapter 2, we assume a polytropic equation of state (2.7). We may then approximate the central sound speed

$$a_c \simeq \left(\frac{\Gamma P_c}{\rho_c}\right)^{1/2} \simeq \left(\frac{\Gamma M}{R}\right)^{1/2}, \tag{3.3}$$

where P_c and ρ_c give the unperturbed neutron star's pressure and density at the center with $P_c \ll \rho_c$. Also, we write the last (rough) equality assuming hydrostatic equilibrium.

We approximate the accretion flow onto the black hole under two opposite limiting regimes by considering whether the neutron star mass $m(r_a)$ contained within the capture radius r_a is smaller or greater than the black hole mass $M_{\rm BH}$. When $m(r_a) > M_{\rm BH}$, we ignore the self-gravity of the neutron star matter, so that the accretion is described by Bondi accretion (see Bondi (1952) and Michel (1972); see also Shapiro and Teukolsky (2004) for a textbook treatment). In the other case $m(r_a) < M_{\rm BH}$, we cannot ignore the self-gravity of the star, so the evolution produces an accretion process that leads to catastrophic dynamical collapse.

We define $m(r)$ as the neutron star mass within the radius r, so that $M = m(R)$, we have

$$m(r) \simeq \frac{4\pi}{3}\rho_c r^3 \tag{3.4}$$

n	Γ	δ	δ/Γ^3	λ_s
3.0	4/3	54.2	22.94	0.707
2.5	7/5	23.3	8.45	0.625
2.0	3/2	11.4	3.38	0.500
1.5	5/3	5.99	1.296	0.250
1.0	2.0	3.29	0.411	–
0.5	3.0	1.84	0.068	–

Table 3.1: Values of the central condensation δ and the combination Γ^3/δ for Newtonian polytropes with polytropic index n and adiabatic index $\Gamma = 1 + 1/n$. For soft equations of state with $\Gamma \leq 5/3$ we also include the accretion eigenvalues λ_s as given by Eq. (2.15). For stiff equations of state with $\Gamma > 5/3$, we find the relativistic accretion eigenvalue $\lambda_{\rm GR}$ following Chapter 2; see also Section 3.4 below.

for sufficiently small r. We then compute the crucial mass ratio,

$$\frac{m(r_a)}{M_{\rm BH}} \simeq \frac{4\pi}{3}\,\frac{M_{\rm BH}^2\rho_c}{a_c^6} \simeq \frac{4\pi}{3}\,\frac{M_{\rm BH}^2\rho_c R^3}{\Gamma^3 M^3}. \tag{3.5}$$

We now write

$$\rho_c = \delta\,\bar{\rho} = \delta\,\frac{3M}{4\pi R^3}, \tag{3.6}$$

where $\bar{\rho}$ is the unperturbed star's mean density, and the factor δ measures its central concentration, $\delta = \rho_c/\bar{\rho}$. In Table 3.1, we list values of δ for various Newtonian polytropes of index n with adiabatic index $\Gamma = 1 + 1/n$. Inserting (3.6) into (3.5) we now have

$$\frac{m(r_a)}{M_{\rm BH}} \simeq \frac{\delta}{\Gamma^3}\,\left(\frac{M_{\rm BH}}{M}\right)^2. \tag{3.7}$$

For large black hole masses $M_{\rm BH} \sim M$ and soft equations of state $\Gamma \leq 5/3$ for which δ/Γ^3 in Table 3.1 is large, we see that $m(r_a) \sim M_{\rm BH}$. For black holes that start with initial mass $M_{\rm BH} \ll M$, most of the accretion process is under the regime $m(r_a) \ll M_{\rm BH}$, and therefore is described as quasistatic Bondi accretion. Only in the short final epoch will the black hole accrete dynamically under the regime $m(r_a) \sim M_{\rm BH}$. We will treat the two cases separately in the following sections, namely for Bondi accretion in Section 3.1.1 and for dynamical accretion in Section 3.1.2.

3.1.1 Bondi accretion: $m(r_a) \ll M_{\rm BH}$

In this case, the gravitational forces are dominated by the black hole which leads us to ignore the self-gravity of the neutron star fluid within the capture radius r_a. In this case, the accretion process is adiabatic Bondi accretion as outlined in Bondi (1952), and the rate is given by

$$\dot{M}^{\star}_{\rm BH} = -\dot{M}^{\star} = 4\pi\lambda_{\rm GR}\left(\frac{M_{\rm BH}}{a^2_{\star}}\right)^2 \rho_{\star} a_{\star}. \tag{3.8}$$

Recall from Chapter 2, $\lambda_{\rm GR}$ is a dimensionless "accretion eigenvalue". Here, the $\star$ symbol denotes quantities as measured by a "local asymptotic observer" meaning far from the black hole but well within the neutron star, i.e. at a radius r with $M_{\rm BH} \ll r \ll R$ where we assume geometrized units with $G = c = 1$. Furthermore, the dot in the accretion rate represents a derivative with respect to the time as measured by the local asymptotic observer. We assume that the density $\rho_{\star}$ and sound speed $a_{\star}$ approach constants, and the flow speed $u_{\star}$ approaches zero as $r \gg r_a$. Typically, this region resides in the nearly homogeneous core of the neutron star. We discuss how this local accretion rate compares to the mass accretion rate as measured by an observer far outside the neutron star in Section 4.3.2.

As outlined in Chapter 2, these eigenvalues can be found under a Newtonian treatment for soft equations of state, but stiff equations of state require a relativistic treatment. We recall that the relativistic accretion eigenvalue $\lambda_{\rm GR}$ given by (2.12) depends on Γ as well as the critical and asymptotic sound speed a_s and a_{∞} respectively.

Assuming that the capture radius r_a is sufficiently small, $r_a \ll R$, we can approximate the fluid variables as observed by the local observer, $\rho_{\star}$ and $a_{\star}$, as the values at the center of the unperturbed neutron star ρ_c and a_c. Now, the accretion rate becomes

$$\dot{M}^{\star}_{\rm BH} = -\dot{M}^{\star} = 4\pi\lambda_{\rm GR}\frac{M^2_{\rm BH}}{a^3_c}\rho_c, \tag{3.9}$$

from which we can estimate the accretion timescale $\tau_{\rm acc}$

$$\tau_{\rm acc} \equiv \frac{M_{\rm BH}}{\dot{M}^{\star}_{\rm BH}} \simeq \frac{a_c^3}{4\pi\lambda_{\rm GR} M_{\rm BH}\rho_c} = \frac{\Gamma^{3/2}}{3\delta\lambda_{\rm GR}} \frac{M^{1/2}R^{3/2}}{M_{\rm BH}} \tag{3.10}$$

where we have used (3.3) and (3.6) in the last step. The above equation estimates the initial time it takes for the black hole to double its mass. This is the longest epoch of the neutron star consumption because the black hole mass and consequently its accretion rate (3.9) are the smallest they will be during the process. We divide by the neutron star mass to obtain a non-dimensional quantity and rewrite our result as

$$\frac{\tau_{\rm acc}}{M} \simeq \frac{\Gamma^{3/2}}{3\delta\lambda_{\rm GR}} \left(\frac{R}{M}\right)^{3/2} \left(\frac{M}{M_{\rm BH}}\right). \tag{3.11}$$

Note that $\tau_{\rm acc}/M \to \infty$ as $M_{\rm BH}/M \to 0$. Another option is to express the accretion timescale in terms of the neutron star's dynamical collapse timescale

$$\tau_{\rm dyn} \simeq \frac{\gamma}{(4\pi\rho_c/3)^{1/2}} = \frac{\gamma}{\delta^{1/2}} \left(\frac{R}{M}\right)^{3/2} M, \tag{3.12}$$

where γ is a factor of order unity and where we have used (3.6). Combining (3.10) and (3.12) we obtain a second non-dimensional quantity

$$\frac{\tau_{\rm acc}}{\tau_{\rm dyn}} \simeq \frac{\Gamma^{3/2}}{\delta^{1/2}\lambda_{\rm GR}\gamma} \left(\frac{M}{M_{\rm BH}}\right). \tag{3.13}$$

Again we have $\tau_{\rm acc}/\tau_{\rm dyn} \to \infty$ as $M_{\rm BH}/M \to 0$. We will calculate $\tau_{\rm acc}$ more carefully in Section 3.3 below.

3.1.2 Dynamical accretion: $m(r_a) \sim M_{\rm BH}$

As mentioned before, we cannot ignore the self-gravity of the star in the case of dynamical accretion. We begin by generalizing the definition of the capture radius (3.1) to include

the mass inside the critical radius $m(r_{\rm crit})$ in addition to the mass of the black hole $M_{\rm BH}$. Thus, we define a critical radius

$$r_{\rm crit} = \frac{m(r_{\rm crit}) + M_{\rm BH}}{a_c^2}. \tag{3.14}$$

Using (3.4), we can rewrite (3.14) as

$$\frac{4\pi}{3}\rho_c r_{\rm crit}^2 \left(1 + \frac{M_{\rm BH}}{m(r_{\rm crit})}\right) = a_c^2. \tag{3.15}$$

We can now express the black hole accretion rate as the area of a sphere with the critical radius, $4\pi r_{\rm crit}^2$, times the mass flux across the sphere, $\rho_c u_c$. As in typical Bondi flows, we assume that the fluid speed at the critical radius, u_c, is comparable to the sound speed a_c, which gives us

$$\dot{M}_{\rm BH}^{\star} \simeq 4\pi r_{\rm crit}^2 \rho_c a_c = 3a_c^3 \left(1 + \frac{M_{\rm BH}}{m(r_{\rm crit})}\right)^{-1}, \tag{3.16}$$

where we have used (3.15) in the last equality. The corresponding accretion timescale is then given by

$$\tau_{\rm acc} = \frac{M_{\rm BH}}{\dot{M}_{\rm BH}} \simeq \frac{M_{\rm BH}}{3\Gamma^{3/2}} \left(\frac{R}{M}\right)^{3/2} \left(1 + \frac{M_{\rm BH}}{m(r_{\rm crit})}\right), \tag{3.17}$$

or

$$\frac{\tau_{\rm acc}}{\tau_{\rm dyn}} \simeq \frac{\delta^{1/2}}{3\gamma\Gamma^{3/2}} \frac{M_{\rm BH}}{M} \left(1 + \frac{M_{\rm BH}}{m(r_{\rm crit})}\right), \tag{3.18}$$

where we have approximated the dynamical timescale $\tau_{\rm dyn}$ as in (3.12).

Now we evaluate Eq. (3.18) in two limits. In the limit $M_{\rm BH} \sim m(r_{\rm crit})$, which gives us $M_{\rm BH} \sim M$ by (3.7), we notice that the accretion timescale $\tau_{\rm acc}$ is comparable to the dynamical timescale $\tau_{\rm dyn}$ given by (3.12). In the opposite limit, $M_{\rm BH} \gg m(r_{\rm crit})$, the critical radius $r_{\rm crit}$ defined in (3.14) reduces to r_a defined in (3.1). We now approximate

$$\frac{M_{\rm BH}}{m(r_{\rm crit})} \simeq \frac{3M_{\rm BH}}{4\pi\rho_c r_a^3} = \frac{3a_c^6}{4\pi\rho_c M_{\rm BH}^2} = \frac{\Gamma^3}{\delta} \left(\frac{M}{M_{\rm BH}}\right)^2, \tag{3.19}$$

where we use (3.3) and (3.6) in the last equality. We recover the Bondi accretion timescale (3.13) up to factors of unity as expected when we insert (3.19) into (3.18).

3.2 Effects of stellar evolution

In the previous section, our simple estimates for the accretion timescales, (3.13) and (3.18), ignore several effects of stellar evolution. Namely, our estimates ignore the fact that the accretion rates change as the black hole mass $M_{\rm BH}$ increases, and that the structure of the neutron star changes as accretion progresses. To approximate the effects of this secular "stellar evolution", we assume that, while the star loses mass to the black hole, it adjusts quasistatically to a new equilibrium configuration while keeping its total Newtonian energy E constant. We now write this energy as

$$E = -\alpha \frac{M M_{\rm BH}}{R} - \frac{3\Gamma - 4}{5\Gamma - 6} \frac{M^2}{R}. \tag{3.20}$$

The first term accounts for the interaction between the stellar gas and the black hole, with α being a constant that depends on Γ, $\alpha = \alpha(\Gamma)$, and the second term describes the neutron star's self-energy (see Eq. 3.3.10 in Shapiro and Teukolsky (2004)).

We evaluate (3.20) at the initial time, as denoted by (0), and have

$$E = -\alpha \frac{M(0) M_{\rm BH}(0)}{R(0)} - \frac{3\Gamma - 4}{5\Gamma - 6} \frac{M(0)^2}{R(0)}. \tag{3.21}$$

By our assumptions, our expressions for energy (3.20) and (3.21) must be identical, so we can equate them and solve for R to find

$$R = \frac{M}{M(0)} \frac{\alpha M_{\rm BH} + (3\Gamma - 4) M/(5\Gamma - 6)}{\alpha M_{\rm BH}(0) + (3\Gamma - 4) M(0)/(5\Gamma - 6)} R(0). \tag{3.22}$$

We now approximate our black hole mass $M_{\rm BH} \ll M$, so (3.22) reduces to

$$R \simeq \left(\frac{M}{M(0)}\right)^2 R(0). \tag{3.23}$$

Using (3.23) in (3.3) then yields

$$a_c \simeq \left(\frac{\Gamma M(0)}{R(0)}\right)^{1/2} \left(\frac{M(0)}{M}\right)^{1/2}, \tag{3.24}$$

while (3.6) gives

$$\rho_c \simeq \delta \, \frac{3M(0)}{4\pi R(0)^2} \left(\frac{M(0)}{M}\right)^5. \tag{3.25}$$

We insert (3.24) and (3.25) into the Bondi accretion rate (3.8) which yields

$$\dot{M} = -\frac{3\lambda_{\rm GR}\,\delta}{\Gamma^{3/2}} \, \frac{(M_{\rm BH}(0) + M(0) - M)^2}{M(0)^{1/2} R(0)^{3/2}} \left(\frac{M}{M(0)}\right)^{-7/2} \tag{3.26}$$

where we have expressed the black-hole mass $M_{\rm BH}$ in terms of the evolving neutron star mass M as

$$M_{\rm BH} = M_{\rm BH}(0) + M(0) - M. \tag{3.27}$$

Our estimate for Bondi accretion (3.26) to leading order does not depend on the parameter α for $M_{\rm BH} \ll M$ meaning the accretion rate does not depend on the interaction between the stellar gas and black hole. We note that the last factor in (3.26) accounts for stellar evolution.

3.3 Accretion times

Using our approximations accounting for stellar evolution, we can compute the neutron star lifetime, i.e. accretion time, by integrating Eq. (3.26). To make our integration

easier, we introduce the useful dimensionless quantities,

$$y_0 \equiv \frac{M_{\rm BH}(0) + M(0)}{M(0)}, \qquad y \equiv \frac{M}{M(0)}, \tag{3.28}$$

and

$$T \equiv \frac{3\lambda_{\rm GR}\,\delta}{\Gamma^{3/2}} \left(\frac{M(0)}{R(0)^3}\right)^{1/2} t. \tag{3.29}$$

Then we may rewrite (3.26) as

$$\frac{dy}{dT} = -(y_0 - y)^2\, y^{-7/2}. \tag{3.30}$$

As in (3.26), the last factor accounts for stellar evolution. Now we consider two cases for the timescale: without stellar evolution and with stellar evolution.

3.3.1 Without stellar evolution

Ignoring stellar evolution, our expression (3.30) reduces to

$$\frac{dy}{dT} = -(y_0 - y)^2, \tag{3.31}$$

which we can integrate to find

$$[T]_i^f = \left[\frac{1}{y - y_0}\right]_i^f. \tag{3.32}$$

We use square brackets here as a reminder to insert the limits of integration. We choose $T_i = 0$ to be our initial time and we have $y_i = 1$. Then using (3.27) we have

$$T_f = \frac{1}{y_f - y_0} - \frac{1}{1 - y_0} = \frac{M(0)}{M_{\rm BH}(0)} - \frac{M(0)}{M_{\rm BH}} \tag{3.33}$$

where $M_{\rm BH}$ is the black hole mass at time T_f. Now to find the total accretion time, we set the final neutron star mass to zero, i.e. we choose $y_f = 0$. Assuming that $M_{\rm BH}(0) \ll M(0)$ and recalling (3.29), we find

$$\frac{\tau_{\rm acc}}{M(0)} = \frac{\Gamma^{3/2}}{3\delta\lambda_{\rm GR}} \left(\frac{R(0)}{M(0)}\right)^{3/2} \left(\frac{M(0)}{M_{\rm BH}(0)}\right), \tag{3.34}$$

which is identical to the estimate of the timescale without an integration (3.11), as expected.

3.3.2 With stellar evolution

We now determine the accretion timescale with stellar evolution by repeating the above exercise and including the last factor in (3.30). In this case, the integral can be carried out as outlined in Appendix B. Again we choose $y_i = 1$ at $T_i = 0$, as well as $y_f = 0$ in order to find the accretion time $T_f = T_{\rm acc}$, we obtain

$$T_{\rm acc} = \frac{5}{2} + \frac{4}{3}y_0 + 6y_0^2 + \frac{y_0^3}{y_0 - 1} - 7y_0^{5/2} \ln\left(\frac{y_0^{1/2} + 1}{y_0^{1/2} - 1}\right). \tag{3.35}$$

We may alternatively introduce

$$y_{h0} = y_0 - 1 = \frac{M_{\rm BH}(0)}{M(0)} \tag{3.36}$$

and rewrite (3.35) as

$$T_{\rm acc} \;=\; 7y_{h0}^2 + \frac{49}{3}y_{h0} + \frac{161}{15} + \frac{1}{y_{h0}} - \frac{7}{2}(y_{h0} + 1)^{5/2} \ln\frac{\sqrt{1 + y_{h0}} + 1}{\sqrt{1 + y_{h0}} - 1}. \tag{3.37}$$

Under the limit that $y_{h0} \to 0$, we note that the $1/y_{h0}$ term dominates $T_{\rm acc}$ which leads us to recover the same accretion time $t_{\rm acc}$ as in Eq. (3.34). Since most of the accretion time is spent during early times, when the neutron star mass and radius does not change

appreciably, stellar evolution is not important, and hence this result is not very surprising. However, at late times, the accretion process and the corresponding adjustments in the stellar structure will effect the accretion time, as shown in (3.37).

We consider a concrete example with $M = 1M_\odot$. In geometrized units, $1M_\odot \simeq 1.4$ km $\simeq 5$ μs which gives us

$$\tau_{\rm acc} \sim \left(\frac{R(0)}{M(0)}\right)^{3/2} \left(\frac{M(0)}{M_{\rm BH}(0)}\right) 10^{-5} \text{ s}, \tag{3.38}$$

ignoring factors of order unity. We see that the accretion time for a main sequence star with $R \simeq 10^5 M_\odot$ if $M_{\rm BH}(0) \lesssim 10^{-15} M_\odot$ will exceed the Hubble time $1/H_0 \sim 4.5 \times 10^{17}$ s where H_0 is the Hubble constant. For our purposes, we consider a neutron star $R \simeq 10 M_\odot$ which gives a significantly smaller accretion timescale. Therefore, we observe that black holes as small as $M_{\rm BH}(0) \gtrsim 10^{-21} M_\odot$ result in an accretion time well within the Hubble time.

3.4 Fiducial neutron star model

To compare with our numerical results presented in Chapter 4, we consider a fiducial neutron star model in stable equilibrium with a central rest-mass density of $\rho_{0c} = 0.2\, K^{-n}$. The star is governed by a polytopic equation of state (2.7) with $\Gamma = 2$, i.e. $n = 1$, and the equilibrium model was found through solving the Tolman-Oppenheimer-Volkoff (TOV) equations as given by Tolman (1939) and Oppenheimer and Volkoff (1939). We list detailed properties for our fiducial neutron star model in Table 3.2.

We observe that $K^{n/2}$ has units of length in geometrized units. Therefore, we are able to rescale any physical quantities with the appropriate power of K and introduce

	Rwrt[1] K	Rwrt M	Rwrt M^{max} model	Physical units
ρ_{0c}[2]	$\tilde{\rho}_{0c} = 0.2$	$M^2\rho_{0c} = 0.00495$	$\rho_{0c}/\rho_{0c}^{\max} = 0.629$	3.41×10^{15} g/cm^3
ρ_c[3]	$\tilde{\rho}_c = 0.24$	$M^2\rho_{0c} = 0.0059$	$\rho_c/\rho_c^{\max} = 0.572$	4.09×10^{15} g/cm^3
R[4]	$\tilde{R} = 0.865$	$R/M = 5.50$	$R/R^{max} = 1.13$	10.8 km
$r_{\rm iso}$[5]	$\tilde{r}_{\rm iso} = 0.699$	$r_{\rm iso}/M = 4.45$	$r_{\rm iso}/r_{\rm iso}^{\max} = 1.19$	8.73 km
M[6]	$\tilde{M} = 0.157$	$M/M = 1$	$M/M^{\max} = 0.959$	2.80×10^{33} g
M_0[7]	$\tilde{M}_0 = 0.176$	$M_0/M = 1.12$	$M_0/M_0^{\max} = 0.954$	3.14×10^{33} g
ψ_c[8]	$\psi_c = 1.27$	$\psi_c = 1.27$	$\psi_c/\psi_c^{\max} = 0.933$	1.27
α_c[9]	$\alpha_c = 0.570$	$\alpha_c = 0.570$	$\alpha_c/\alpha_c^{\max} = 1.23$	0.570

[1] Rescaled with respect to
[2] Central rest-mass density
[3] Central mass-energy density
[4] Areal radius
[5] Isotropic radius
[6] Gravitational mass
[7] Rest mass
[8] Central conformal factor
[9] Central lapse function

Table 3.2: Parameters for our fiducial $\Gamma = 2$, $n = 1$ polytropic neutron star model without a black hole. Here, the lapse function α is the value obtained from integrating the TOV equations, and is different from the 1+log lapse adopted in our numerical evolution calculations given by Eq. (4.11).

non-dimensional quantities, eg.

$$\begin{aligned} \tilde{\rho} &\equiv K^n\rho, \qquad \tilde{R} \equiv K^{-n/2}R, \\ \tilde{\rho}_0 &\equiv K^n\rho_0, \qquad \tilde{M} \equiv K^{-n/2}M, \end{aligned} \tag{3.39}$$

and similar for other quantities. The "tilde" variables are those scaled with respect to K and are listed in the second column of Table 3.2. In the third column, we list variables scaled with respect to the neutron star's gravitational mass M, and similarly, the fourth column lists variables scaled with respect to maximum mass configuration. We note in particular for our fiducial neutron star model that $M/M^{\max} = 0.959$ where $M^{\max}$ is the maximum gravitational mass of a spherical star with our adopted equation of state. In the final column, we list physical values of our variables where we assume $M = 1.4\,M_\odot$, in which case K takes the value $K = (1.4\,M_\odot/\tilde{M})^2 \simeq 156$ km^2.

As mentioned at the end of Chapter 2, we wish to find the accretion rate and asso-

ciated quantities for our fiducial neutron star model, and we do so using the parameters given in Table 3.2. First we compute the central sound speed to be

$$a_c = 0.534. \tag{3.40}$$

Then, we identify the neutron star's central density and sound speed to be the same as the asymptotic values for the Bondi accretion onto the black hole as we have done previously. Following Chapter 2 and using (2.12), we compute the accretion eigenvalue

$$\lambda_{\rm GR} = 1.29. \tag{3.41}$$

We then insert the above values into the Bondi accretion rate (3.8) and obtain

$$\dot{M}^{\star}_{\rm BH} = 21.24\, \tilde{M}^2_{\rm BH}. \tag{3.42}$$

We notice that our result is not significantly larger than the minimum steady state accretion rate for $\Gamma = 2$ given by (2.34) in terms of our rescaled mass,

$$\dot{M}^{\star}_{\rm BH,min} = 9.29\, \tilde{M}^2_{\rm BH}. \tag{3.43}$$

Adopting the above value of K, and recalling that, in geometrized units, $M_\odot \simeq 5\times10^{-6}$ s, we can evaluate (3.43) to yield

$$\dot{M}^{\star}_{\rm BH,min} = 7.33 \times 10^{-9}\, \frac{M_\odot}{\rm yr} \left(\frac{M_{\rm BH}}{10^{-10} M_\odot} \right)^2. \tag{3.44}$$

Chapter 4

Numerical Simulations

This chapter outlines the process to numerically determine the accretion rate and accretion time of a nonspinning black hole evolving at the center of a nonrotating, spherical neutron star in hydrostatic equilibrium. We extend the work of East and Lehner (2019) by expanding on their relatively limited range of large masses $M_{\rm BH}/M \geq 10^{-2}$ where M is the neutron star mass. The numerical evolutions are performed by the code outlined in Baumgarte et al. (2013), (2015) using the Runge-Kutta method to solve Einstein's equations under the Baumgarte-Shapiro-Shibata-Nakamura (BSSN) formulation. In particular, we adopt spherical polar coordinates with a logarithmic radial coordinate in order to allow mass ratios as small as $M_{\rm BH}/M \simeq 10^{-9}$.

4.1 Initial data profile

To begin our evolutions, we construct an initial data profile describing a black hole at the center of a neutron star. We do so by generalizing the puncture method as outlined in Brandt and Brügmann (1997) to allow for the presence of matter. To do so, we solve the Hamiltonian constraint under the assumption that the initial slice is conformally flat, i.e. we assume that $\gamma_{ij} = \psi^4 \eta_{ij}$ where γ_{ij} is the spatial metric and ψ is the conformal factor. We also assume a moment of time symmetry, so that the extrinsic curvature

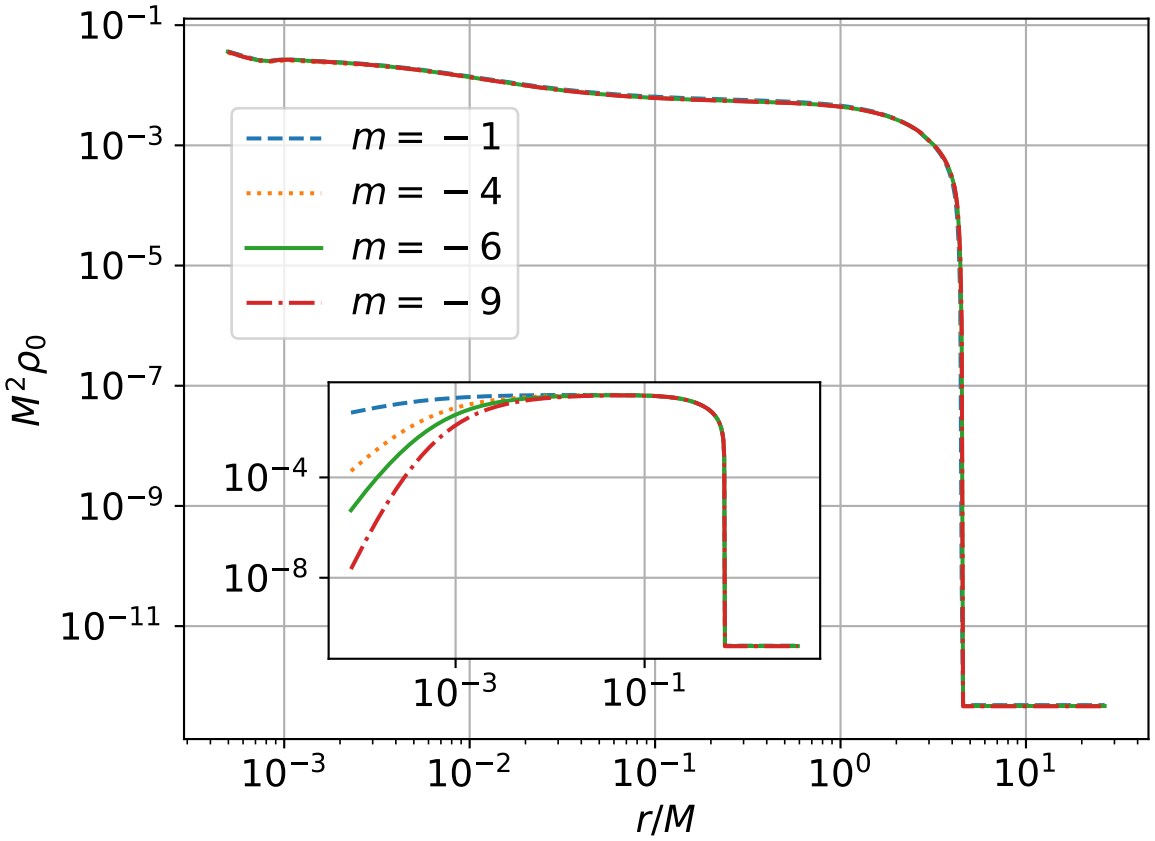

Figure 4.1: The rest-mass density profiles as a function of isotropic radius r for our fiducial neutron star model with an embedded black hole with puncture mass $\tilde{\mathcal{M}} = 10^{-3}$, so $\tilde{M}_{\rm BH}(0) = 1.267 \times 10^{-3}$, and $M_{\rm BH}(0)/M(0) = 8.03 \times 10^{-3}$ for various values of m from Eq. (4.2). Inset: Initial rest-mass density profiles. We clearly see that these profiles depend on the choice of conformal exponent m as they all give different initial profiles. Outset: Evolved rest-mass density profiles. Once they reach a quasi-equilibrium, they all evolve to the same density profile. In this figure and several others, we have removed a few of the innermost grid points as they were a result of numerical noise from the puncture singularity.

vanishes $K_{ij} = 0$. The Hamiltonian constraint then becomes

$$\bar{D}^2\psi = -2\pi\psi^5\rho. \tag{4.1}$$

Here, $\bar{D}^2$ is the flat Laplace operator, and $\rho = n_a n_b T^{ab}$ is the energy density as observed by an observer whose four-velocity is the normal vector n^a. We also rescale the density according to

$$\rho = \psi^m \bar{\rho}, \tag{4.2}$$

where $\bar{\rho}$ is a conformally rescaled density, and m is a yet-to-be-determined exponent. We notice that $m = -6$ is an appealing option because the proper integral over the density is invariant if $\bar{\rho}$ is fixed,

$$\int \psi^6 \rho \, d^3x = \int \bar{\rho} \, d^3x. \tag{4.3}$$

As shown in the inset of Fig. 4.1, different conformal exponents m lead to different initial data profiles, but they all evolve to the same data profile. Therefore, we are free to choose the convenient $m = -6$ as our conformal exponent for all of our simulations.

Assuming we have constructed solutions to the TOV equations in isotropic coordinates (see Oppenheimer and Volkoff (1939) and Tolman (1939)), we obtain radial profiles of the conformal factor $\psi_{\rm NS}$ and mass-energy density $\rho_{\rm NS}$ for the equilibrium neutron star by itself. These functions $\psi_{\rm NS}$ and $\rho_{\rm NS}$ satisfy the Hamiltonian constraint (4.1) with

$$\bar{D}^2\psi_{\rm NS} = -2\pi\psi_{\rm NS}^5\rho_{\rm NS}. \tag{4.4}$$

We then identify the conformally rescaled density as

$$\bar{\rho} = \psi_{\rm NS}^{-m} \, \rho_{\rm NS}. \tag{4.5}$$

Now we modify our solution to account for the presence of a black hole at the center of

our neutron star. To do so, we rewrite the conformal factor as a sum of the contributions from the neutron star and black hole with a correction u,

$$\psi = \psi_{\rm NS} + \psi_{\rm BH} + u. \tag{4.6}$$

Since our solution is non-linear, we are no longer able to use the superposition principle to construct our solution and therefore require the addition of the correction u. We then recast the Hamiltonian constraint as an equation for u and expect the solution u is regular everywhere. In (4.6) we introduce a black hole's contribution to the conformal factor

$$\psi_{\rm BH} = \frac{\mathcal{M}}{2r} \tag{4.7}$$

in isotropic coordinates. We note that the "puncture mass" $\mathcal{M}$ acts as a mass parameter and carries no physical significance. Later, we will give expressions for the black hole's horizon, or irreducible, mass. Now we insert the conformal factor (4.6) into the Hamiltonian constraint (4.1), noticing that $\bar{D}^2\psi_{\rm BH} = 0$, and are left with

$$\bar{D}^2\psi_{\rm NS} + \bar{D}^2 u = -2\pi \left(\psi_{\rm NS} + \psi_{\rm BH} + u\right)^{5+m} \bar{\rho}, \tag{4.8}$$

or, inserting (4.4),

$$\bar{D}^2 u = -2\pi \left\{\left(\psi_{\rm NS} + \psi_{\rm BH} + u\right)^{5+m} - \psi_{\rm NS}^{5+m}\right\} \bar{\rho}. \tag{4.9}$$

Noticing that $\psi_{\rm BH} \to \infty$ as $r \to 0$, we note that our previous choice $m = -6$ keeps the right-hand side of (4.9) regular (See Appendix C in Richards et al. (2021b) for an approximate, analytical solution to Eq. (4.9)).

Now we are left to find regular solutions to Eq. (4.9) under the boundary condition $u \propto 1/r$ for large r in order to consider the addition of the first-order monopole to the gravitational potential. In order to solve the non-linear equation, we adopt an iterative

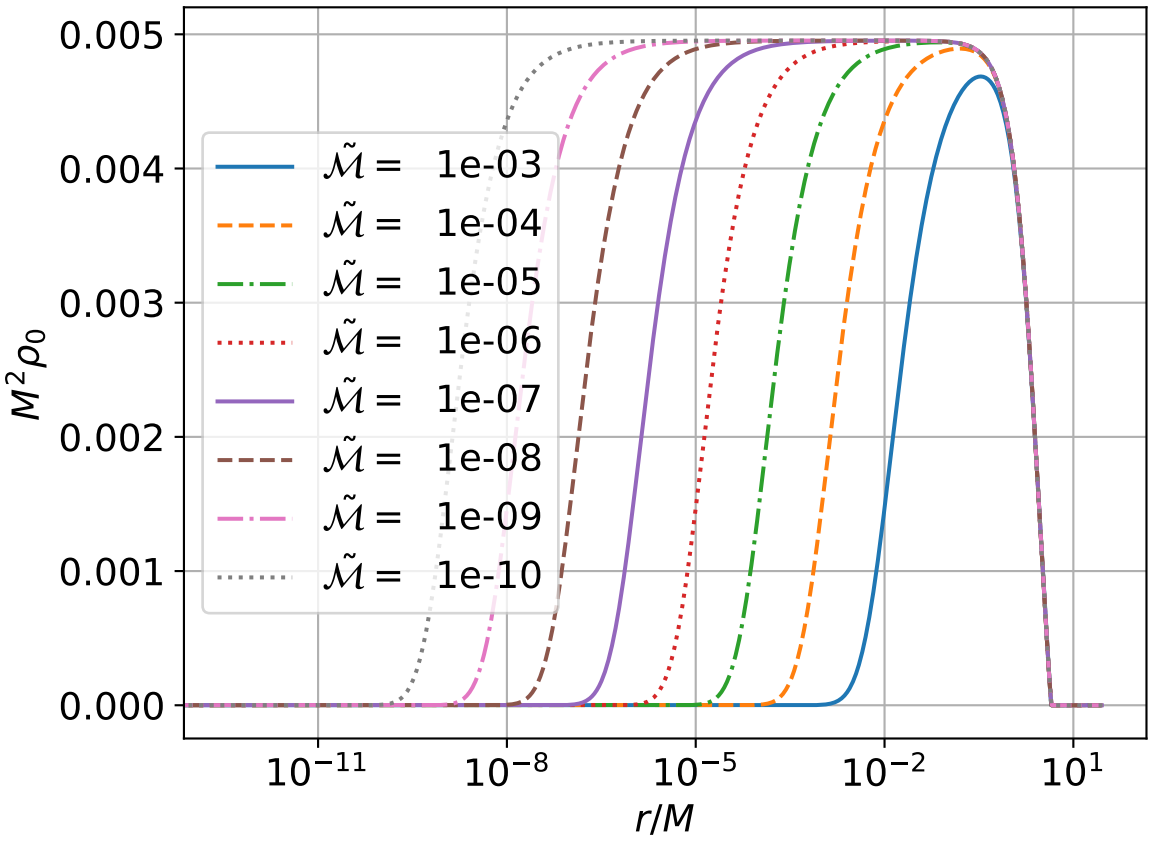

Figure 4.2: Profiles of initial rest-mass density ρ_0 as a function of isotropic radius r for our fiducial neutron star model with an embedded black hole for various puncture masses $\mathcal{M}$. Here, and unless stated otherwise, we choose $m = -6$ in Eq. (4.2). Due to the use of a logarithmic scale, we are able to resolve the vastly different length scales between the neutron star and black hole, even the smallest black holes.

approach. From this solution of u, we are able to compute the new, physical energy density from

$$\rho = \psi^m \bar{\rho} = \left(\frac{\psi_{\rm NS} + \psi_{\rm BH} + u}{\psi_{\rm NS}} \right)^m \rho_{\rm NS}. \tag{4.10}$$

We recognize that for $m < 0$ we will have $\rho \to 0$ as $r \to 0$ initially.

For our simulations using the code described in Baumgarte et al. (2013), (2015), we implement the above approach to solve Einstein's equations in spherical polar coordinates. We use a logarithmic radial coordinate so that we are able to resolve both the black hole and neutron star without wasting numerical resources, even when $\mathcal{M} \ll M$. In

Figure (4.2), we show density profiles for black holes with varying $\mathcal{M}$ inside our neutron star model which demonstrates our ability to resolve vastly different length scales, even for tiny black hole masses.

4.2 Numerical evolution

We evolve our initial data with a code that solves the Baumgarte-Shapiro-Shibata-Nakamura (BSSN) formulation of Einstein's equations (Nakamura et al. (1987); Shibata and Nakamura (1995); Baumgarte and Shapiro (1999)). We adopt an implementation in spherical polar coordinates (see Baumgarte et al. (2013, 2015) for details and tests; see also Miller and Baumgarte (2017) for tests with Bondi accretion as well as Ruchlin et al. (2018); Mewes et al. (2018, 2020) for other implementations of this approach), using reference-metric formulation to handle coordinate singularities (see, e.g., Bonazzola et al. (2004); Shibata et al. (2004); Brown (2009); Gourgoulhon (2012)). The latest version of our code uses fourth-order finite differencing for all spatial derivatives in Einstein's equations, together with a fourth-order Runge-Kutta time integrator.

We impose coordinates using the "1+log" slicing condition

$$(\partial_t - \beta^i \partial_i)\, \alpha = -2\alpha K \tag{4.11}$$

(see Bona et al. (1995)) for the lapse function α, and a "Gamma-driver" condition for the shift vector β^i (see Alcubierre et al. (2003); Thierfelder et al. (2011)). On our initial slice we choose a "pre-collapsed" lapse with $\alpha = \psi^{-2}$ and zero shift.

For all simulations in this thesis, we use a numerical grid with $N_r = 512$ radial grid points with the outer boundary at $\tilde{r}_{\rm out} = 4$ which is approximately 5.7 times the isotropic radius our of neutron star model. Our grid is logarithmic asymptotically as we use a sinh function to distribute radial grid points. We find this implementation useful because it allows us to resolve vastly different length scales associated with the black hole

and neutron star masses. Adjusting the parameters of this sinh function, we resolve each black hole by approximately 50 grid points, and the smallest grid spacing at the center of the black hole is approximately 1% of the black hole's isotropic radius or less.

Similar to above, we follow Montero et al. (2014) to adopt a reference-metric formulation in order to implement the equations of relativistic hydrodynamics in spherical polar coordinates. The resulting equations are solved using an HLLE approximate Riemann solver (Harten et al. (1983); Einfeldt (1988)) with a simple monotonized central-difference limiter reconstruction scheme (van Leer (1977)). We solve these equation adopting an ideal gas law

$$P = (\Gamma - 1)\rho_0\epsilon, \tag{4.12}$$

where ϵ is the specific internal energy density, in terms of which the total mass energy density is given by $\rho = \rho_0(1 + \epsilon)$. For our simulations, we focus on $\Gamma = 2$ and refer to East and Lehner (2019) for an analysis of different equations of state.

We give examples of our evolution calculations in Fig. (4.1) showing the density profile evolve for a black hole with puncture mass $\tilde{\mathcal{M}} = 10^{-3}$ at the center of our fiducial neutron star model. From Eq. (4.2), we notice that our initial data depend on our choice of m. However, we observe that, while the initial density profile in the inset of Fig. (4.1) differ, they all evolve to to the same quasi-equilibrium density profile, meaning that the evolution calculations are largely independent of m. Therefore, we feel comfortable in our choice of specifying $m = -6$ for all of our simulations.

4.3 Diagnostics

4.3.1 Black hole mass

A black hole's isolated horizon, or irreducible, mass is given by

$$M_{\rm BH} = \left(\frac{\mathcal{A}}{16\pi}\right)^{1/2}, \tag{4.13}$$

where $\mathcal{A}$ is the proper area of the black hole's event horizon at a given instant of time.

In our evolution simulations, we locate the apparent horizon. We choose to locate the apparent horizon rather than the event horizon because the former requires data only at one instant of time, whereas the latter it is difficult to locate numerically since it requires data for all times. For a textbook analysis of the respective horizons, see Baumgarte and Shapiro (2010). Then, we compute the black hole's proper area and insert it into (4.13), which gives an excellent approximation for the black hole mass, in particular for stationary spacetimes or nearly stationary spacetimes.

We also approximate the initial black hole mass as follows. Our initial data are conformally flat and describe a moment of time symmetry with zero shift, so we write the initial spacetime metric as

$$ds^2 = -\alpha^2 dt^2 + \psi^4 (dr^2 + r^2 d\Omega^2). \tag{4.14}$$

Then, following Eq. (7.22) from Baumgarte and Shapiro (2010) with $A^2 = B^2 = \psi^4$, the expansion of a bundle of outgoing null geodesics orthogonal to a spherical surface of radius r is given by

$$\Theta = \frac{\sqrt{2}}{r\psi^2} \frac{d}{dr} \left(r\psi^2\right). \tag{4.15}$$

Now we assume that u in (4.6) is small (see Appendix C in Richards et al. (2021a)) compared to the neutron star and black hole contributions, so we approximate the conformal

factor as

$$\psi \simeq \psi_{\rm NS} + \psi_{\rm BH} = \psi_{\rm NS} + \frac{\mathcal{M}}{2r}. \tag{4.16}$$

We note that we may approximate $\psi_{\rm NS}$ as constant for r much smaller than the neutron star radius.

Now, to find the black hole's apparent horizon, we set the expansion (4.15) to zero,

$$\frac{d}{dr}\left(r\left(\psi_{\rm NS} + \frac{\mathcal{M}}{2r}\right)^2\right) \simeq \psi_{\rm NS}^2 - \frac{\mathcal{M}^2}{4r^2} = 0 \tag{4.17}$$

or

$$r_{\rm AH} \simeq \frac{\mathcal{M}}{2\psi_{\rm NS}}. \tag{4.18}$$

Evaluating (4.16) at the apparent horizon we then have

$$\psi_{\rm AH} \equiv \psi(r_{\rm AH}) \simeq 2\psi_{\rm NS}. \tag{4.19}$$

Using (4.18) and (4.19), we can now compute the proper area of the apparent horizon from

$$\mathcal{A} = 4\pi\psi_{\rm AH}^4 r_{\rm AH}^2 = 16\pi\psi_{\rm NS}^2\mathcal{M}^2. \tag{4.20}$$

Inserting (4.20) into (4.13) we obtain our result

$$M_{\rm BH} \simeq \psi_{\rm NS}\mathcal{M}, \tag{4.21}$$

where we estimate $\psi_{\rm NS}$ to be the central value of the unperturbed neutron star's conformal factor. We will see that, for $\mathcal{M} \ll M$, Eq. (4.21) gives an excellent approximation for the initial black hole masses (see Table 5.1).

4.3.2 Growth of black hole

In our simulations, we measure black hole accretion of neutron star matter in two different ways, as shown in Fig. (1.1) and Table 5.1.

One method to determine accretion is to directly measure the black hole mass $M_{\rm BH}$ from (4.13) as a function of coordinate time. We will then determine the accretion rate from the slope of this function as shown, for example, in Fig. 4.3. We show the evolution of a black hole embedded in a neutron star, shown as the orange line, along with a black hole with the same mass $M_{\rm BH}(0)$ evolved in vacuum, i.e. without a neutron star, shown as the red dashed line. The black hole evolved in vacuum gives a nearly horizontal slope, demonstrating that our black hole embedded in a neutron star accretes matter from the neutron star, and therefore, its slope is not a product of numerical noise. As we decrease the black hole mass, the corresponding accretion rate becomes increasingly slow (see Eq. (3.8)). Therefore, we can only use this direct measurement of black hole growth for black holes with initial mass $\tilde{M}_{\rm BH}(0) \gtrsim 10^{-4}$ (see red triangles in Fig. 1.1, and Table 5.1).

The slope of curves $M_{\rm BH}(t)$ yields the accretion rate $\dot{M}_{\rm BH}$ where the derivative is taken with respect to the coordinate time t. At large distances from the neutron star, $r \gg R$, the coordinate time agrees with the proper time of a static observer at infinity. Therefore, we use this measure of the accretion rate as the accretion measured by any static observer at infinity. Earlier in Section 3.1, we introduced the accretion rate $\dot{M}^{\star}_{\rm BH}$ observed by a "local asymptotic" observer far from the black hole, but well within the star, $M_{\rm BH} \ll r \ll R$. We therefore take the derivative with respect to the local observer's proper time $\tau_\star$ for the accretion rate $\dot{M}^{\star}_{\rm BH}$ (for a detailed discussion of the effect of considering a local asymptotic observer, see Appendix A from Richards et al. (2021a)). Now, we can relate the two rates $\dot{M}_{\rm BH}$ and $\dot{M}^{\star}_{\rm BH}$ by recognizing that the proper time of the static, local observer advances at a rate $d\tau_\star = \alpha_\star dt$, where $\alpha_\star$ is the lapse

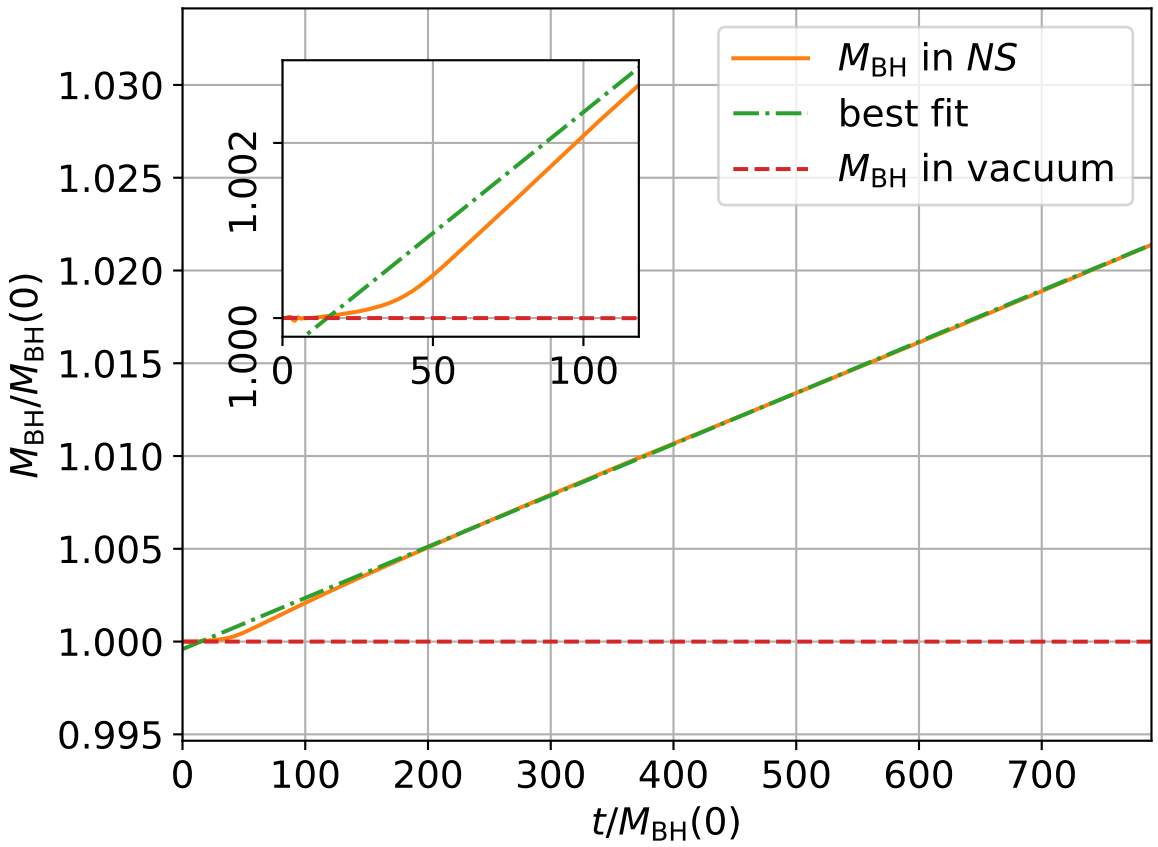

Figure 4.3: Growth of black hole's irreducible mass with respect to coordinate time t given by (4.13) for a black hole embedded in our fiducial neutron star model (orange line) with $\tilde{M}_{\mathrm{BH}}(0) = 1.267 \times 10^{-3}$. The green dot-dashed line gives a linear fit to our numerical data, and we identify its slope as the accretion rate $\dot{M}_{\mathrm{BH}}$. As a way to calibrate numerical error, we include the evolution of a black hole in vacuum, i.e. without a neutron star, with the same mass (red dashed line) and observe a nearly horizontal slope representing zero accretion rate.

function of this local observer. We then have

$$\dot{M}_{\rm BH} = \frac{dM_{\rm BH}}{dt} = \alpha_\star \frac{dM_{\rm BH}}{d\tau_\star} = \alpha_\star \dot{M}^\star_{\rm BH}. \tag{4.22}$$

To interpret this relation, we state that the accretion rate observed by a distant observer $\dot{M}_{\rm BH}$ is red-shifted by the lapse function $\alpha_\star$ with respect to the rate as observed by a local observer $\dot{M}^\star_{\rm BH}$.

See Table 5.1 for accretion rates determined numerically from the growth of the black hole mass.

4.3.3 Rest-mass flux

Another way to compute the accretion rate of the black hole at the center of our fiducial neutron star model is to measure the rate of fluid flow across the black hole horizon. Under the assumption that the accretion is sufficiently slow, we approximate the black hole to be nearly static. We may then follow the treatment in Appendix A from Farris et al. (2010), and compute the flux $\mathcal{F}$ of rest-mass accretion through a sphere $\mathcal{H}$ with radius r from

$$\mathcal{F}(r) = -\int_{\mathcal{H}} \sqrt{-g}\rho_0 u^r d\theta d\phi, \tag{4.23}$$

where g is the determinant of the spacetime metric. We solve the integral under spherical symmetry to obtain

$$\mathcal{F}(r) = -4\pi\alpha\sqrt{\gamma}\rho_0 u^r r^2, \tag{4.24}$$

with $\sqrt{-g} = \alpha\sqrt{\gamma}$, and where γ is the determinant of the spatial metric. We identify this expression as the flux of rest-mass accretion through a sphere of any radius r. When evaluated for a black hole, we compute the flux at the apparent horizon such that

$$\dot{M}_{\rm BH} = \mathcal{F}(r_{\rm hor}). \tag{4.25}$$

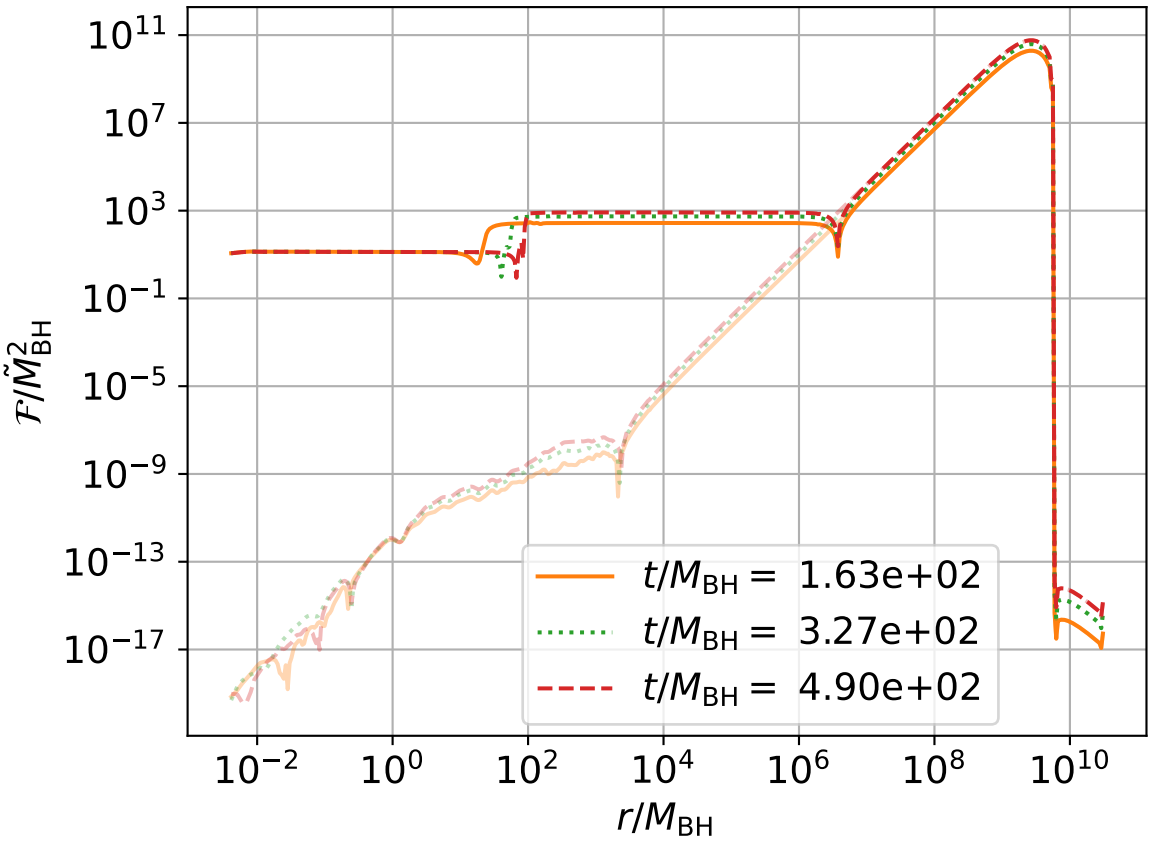

Figure 4.4: Flux profiles (4.24) as a function of isotropic radius r at various instances of time for black hole with initial mass $\tilde{M}_{\rm BH}(0) = 1.267 \times 10^{-10}$ embedded at the center of our fiducial neutron star model. We compute the flux by measuring the flow across the radius r. In the outer parts of the star, we note that the non-zero flux is due to a numerical adjustment of the star because the initial data and numerical grid are not perfectly in equilibrium. In the inner parts of the star, we reach equilibrium accretion onto the black hole as the flux approaches a value independent of both space and time. For comparison, we include the evolution of a neutron star without a black hole (faint lines) which shows the same behavior in the outer parts of the star but very different behavior close to the black hole. We note that we rescale both profiles for a neutron star with and a neutron star without a black hole using $M_{\rm BH}$ from the simulation of a neutron with a black hole.

We expect the flux $\mathcal{F}$ to be independent of the radius for stationary flow. We demonstrate this in Fig. (4.4) where we show profiles of $\mathcal{F}$ at various instances of time for a black hole with initial mass $M_{\rm BH}(0)/M = 7.12 \times 10^{-10}$ inside of our fiducial neutron star model. In particular, we notice that the fluid settles into steady-state accretion onto the black hole in an inner region that grows with time as the flux takes a nearly constant value.

We also include profiles of our fiducial neutron star model without a black hole in Fig. (4.4). Although they have a similar profile in the outer part of the star, where numerical adjustments of the grid dominate the flux $\mathcal{F}$, we notice that the profiles are very different close to the black hole. The difference between the profile in the inner region of the star gives us confidence that the plateau in flux for the neutron star evolving with a black hole represents the steady-state accretion onto the black hole, and not a numerical artifact.

We record our numerical results for these accretion rates in Table 5.1. We note that, like the accretion rate computed in Section 4.3.2, our rate (4.25) represents a rate as measured by an observed far from the neutron star, i.e. at $r \gg R$. In order to compare this rate with the rate observed by a "local aymptotic" observer at $M_{\rm BH} \ll r \ll R$ as computed in Section 3.1, we again require the local observer's lapse function $\alpha_\star$ (see Appendix A from Richards et al. (2021a) for further details).

In Section 4.3.2 we computed the accretion rate from the growth of the black hole's gravitational mass, whereas here we measure the accretion of the rest mass to compute the flux (4.25). We observe in our numerical simulations that the black hole's gravitational mass grows at a rate slightly larger than the rate of rest-mass accretion, presumably because the former includes accretion of other forms of energy as well as rest-mass energy.

Chapter 5

Accretion Results

In this chapter, we will compare our analytical estimates from Chapters 2 and 3 with our numerical results from Chapter 4 for our fiducial neutron star model with black holes of various masses at its center.

5.1 Comparison with Bondi flow

To begin our comparisons, we will look at fluid flow profiles. For our numerical simulations, we focus on data near the black hole at late times so that the fluid has settled into steady state accretion. We compare our numerical results with our estimates from Chapter 2 giving a direct integration of the "relativistic Bondi-equations" (see also Appendix G of Shapiro and Teukolsky (2004)). We recall that these equations describe spherically symmetric, steady-state, adiabatic fluid flow in a Schwarzschild spacetime.

The coordinates in our code are different from the Schwarzschild coordinates used in constructing solutions to steady-state Bondi accretion. Therefore we can only compare scalar quantities, for example rest-mass density, directly. To resolve this issue of comparison, we introduce the "Killing observer", i.e. a static observer with four-velocity aligned with a timelike Killing-vector $\xi^a = \partial/\partial t$. We then compute the "gamma-factor"

W_ξ between an observer moving with the fluid and the "Killing observer",

$$W_\xi = -\frac{\xi^a u_a}{(-\xi^a \xi_a)^{1/2}} = -\frac{u_t}{(-g_{tt})^{1/2}}, \tag{5.1}$$

to give a comparison of an invariant measure of the fluid four-velocity u^a. In Schwarzschild coordinates, we can express this as

$$\begin{aligned} W_\xi = \alpha_{\rm S} u^{t_{\rm S}} &= \left(1 - \frac{2M_{\rm BH}}{r_{\rm S}}\right)^{1/2} u^{t_{\rm S}} \\ &= \left\{1 + \left(1 - \frac{2M_{\rm BH}}{r_{\rm S}}\right)^{-1} (u^{r_{\rm S}})^2\right\}^{1/2}, \end{aligned} \tag{5.2}$$

while, in our code, we evaluate

$$W_\xi = \frac{W(\alpha - \beta_r v^r)}{(\alpha^2 - \beta_r \beta^r)^{1/2}} \tag{5.3}$$

with $W = \alpha u^t$ and

$$v^r \equiv \frac{1}{W}\gamma^r_a u^a = \frac{u^r}{W} + \frac{\beta^r}{\alpha}, \tag{5.4}$$

where v^i is the spatial projection of the four-velocity u^a, divided by W. We note here that static observers must be outside the black hole, and therefore, we can evaluate W_ξ only for $r \gtrsim 2M_{\rm BH}$.

Now, we can finally compare the flux (4.24) found in our code with the accretion rate (3.8) given by the Bondi solution. We give a comparison for a black hole with mass $\tilde{\mathcal{M}} = 10^{-6}$ at coordinate time $t = 1.59 \times 10^3 M_{\rm BH}$ in Fig. 5.1. In the upper two panels showing rest-mass density and the gamma-factor W_ξ respectively, the curves agree very well and are difficult to differentiate. The bottom panel comparing the accretion rates appears to differ more because the analytical estimate is given by a (nearly) constant value. In reality, the accretion rates agree within a fraction of a percent in the vicinity of the black hole, demonstrating that relativistic Bondi accretion excellently describes the

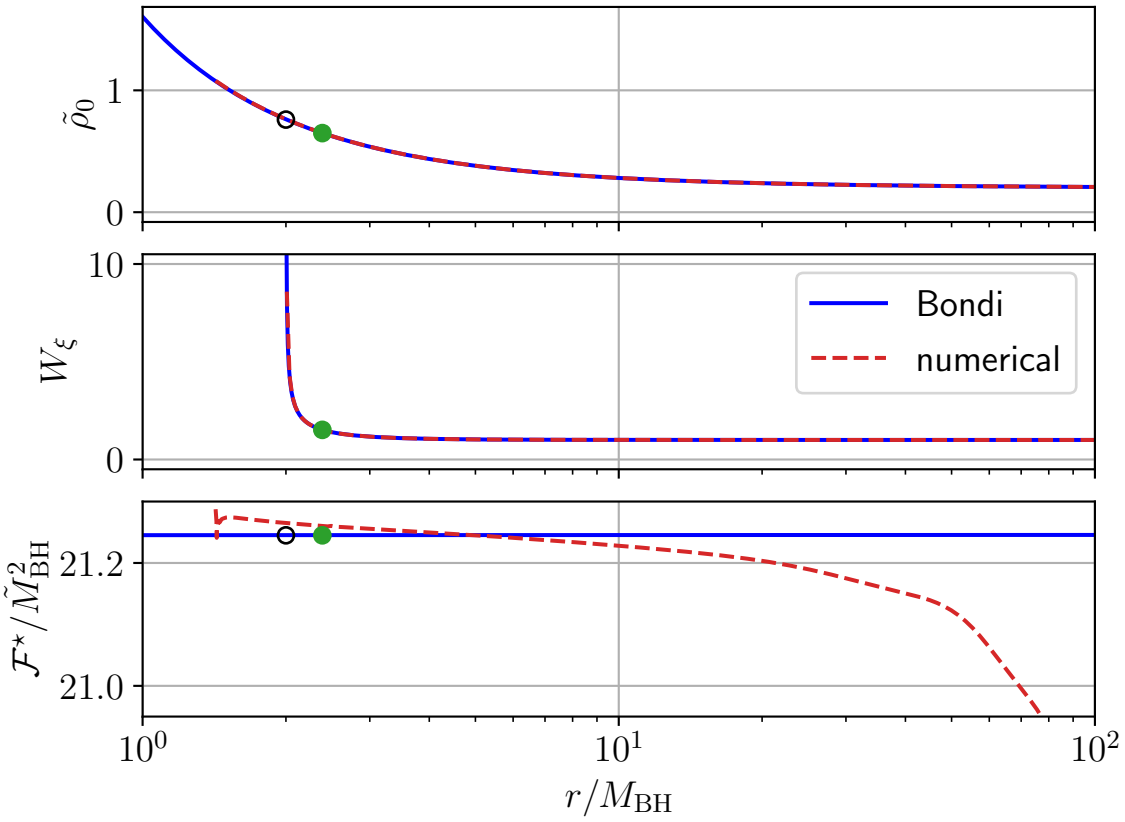

Figure 5.1: Comparison of our numerical fluid flow profiles (dashed red lines) with analytical Bondi accretion (solid blue lines) for our fiducial neutron star model with a black hole with initial mass $\tilde{M}_{\rm BH}(0) = 1.267 \times 10^{-6}$ at time $t = 1.59 \times 10^3 M_{\rm BH}$. The black hole horizon at $r = 2M_{\rm BH}$, where r is the areal radius, is marked by the open black circles. We also mark the critical radius with the solid green dots, giving the location at which the fluid flow becomes supersonic in the Newtonian limit.

accretion rate for an endoparastic black hole at the center of a neutron star.

5.2 Complete consumption

For black holes with small initial masses, the accretion process is too long to simulate numerically. Therefore, we perform simulations of complete consumption of the neutron star only for black holes with initial mass sufficiently large. We give an example of a neutron star completely consumed by a black hole with initial mass $\tilde{M}_{\rm BH}(0) = 0.0126$ in Fig. 5.2. The initial data have a total gravitational Arnowitt-Deser-Misner (ADM) mass of $\tilde{M}_{\rm ADM} = 0.1655$, so that $M_{\rm BH}(0)/M_{\rm ADM} = 0.0761$. We observe that the black hole grows steadily at early times, similar to analytical accretion rate given in Section 3.1.1. Then, the accretion becomes dynamical as described in Section 3.1.2 around $t \simeq 25 M_{\rm ADM}$. Finally, the black hole completely consumes the neutron star and its mass settles to a value within less than 0.1% of the ADM mass, confirming the accuracy of our simulations.

We also provide analytical estimates from Section 3.3.1 and 3.3.2 for the accretion without stellar evolution (dotted line) and with stellar evolution (dashed line) respectively in Figure 5.2. The comparisons between these accretion rates should be considered qualitative for several reasons (see Section IVB in Richards et al. (2021a) for full details). We recall that all analytical estimates in Chapter 3 were made based on rates observed by a static, "local asymptotic observer", and in order to compare the "local" and "global rates", we require the lapse function of a local observer $\alpha_\star$. We are able to determine such a function well for $M_{\rm BH} \ll M$, but for the case $M_{\rm BH} \lesssim M$ it becomes difficult to identify a local lapse function unambiguously. Furthermore, during the late stages of the accretion process, we can no longer define a local, static observer with $M_{\rm BH} \ll r \ll R$. If we were able to follow a black hole with initial mass $M_{\rm BH} \ll M$ to complete consumption, we would observe better agreement in Fig. 5.2 between the results as we increase the number of decades in both time and increasing mass ratio.

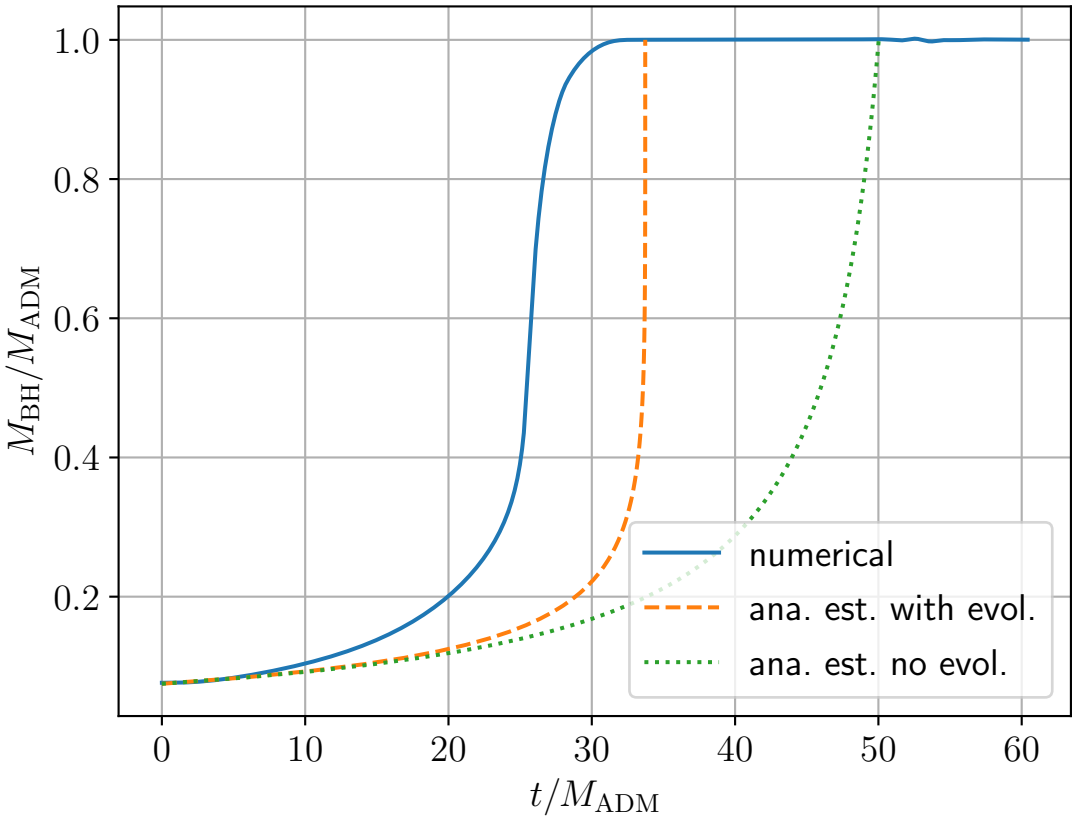

Figure 5.2: Black hole mass $M_{\rm BH}$ as a function of coordinate time t for a simulation leading to complete collapse. We show the numerical results for a black hole with initial mass $\tilde{M}_{\rm BH}(0) = 0.0126$ represented by the solid line. The dashed line represents the analytical estimate accounting for stellar evolution (B.16), while the dotted line represents the analytical estimate ignoring stellar evolution (3.33). After the black hole has consumed the entire neutron star at late times, we observe that the black hole mass agrees to high accuracy with the initial total gravitational mass $M_{\rm ADM}$. In this comparison we have adopted the value $\alpha_\star \simeq 0.623$.

$\tilde{\mathcal{M}}$[1]	$\tilde{M}_{\rm BH}(0)$[2]	$\alpha_\star$[3]	$\dot{M}_{\rm BH}/\alpha_\star{}^4$	$\mathcal{F}(r_{\rm AH})/\alpha_\star{}^5$	$\dot{M}^\star_{\rm BH}$[6]
10^{-3}	1.267×10^{-3}	0.616	4.58×10^{-5}	3.44×10^{-5}	3.41×10^{-5}
10^{-4}	1.267×10^{-4}	0.619	4.67×10^{-7}	3.42×10^{-7}	3.41×10^{-7}
10^{-5}	1.267×10^{-5}	0.622	–	3.41×10^{-9}	3.41×10^{-9}
10^{-6}	1.267×10^{-6}	0.623	–	3.40×10^{-11}	3.41×10^{-11}
10^{-7}	1.267×10^{-7}	0.623	–	3.42×10^{-13}	3.41×10^{-13}
10^{-8}	1.267×10^{-8}	0.623	–	3.43×10^{-15}	3.41×10^{-15}
10^{-9}	1.267×10^{-9}	0.623	–	3.43×10^{-17}	3.41×10^{-17}
10^{-10}	1.267×10^{-10}	0.623	–	3.43×10^{-19}	3.41×10^{-19}

[1] Black hole puncture mass $\tilde{\mathcal{M}} = K^{-1/2}\mathcal{M}$ in our initial data; see Section 4.1.
[2] Initial irreducible mass $\tilde{M}_{\rm BH}(0) = K^{-1/2}M_{\rm BH}(0)$ of the black hole; see Section 4.3.1.
[3] Lapse of a "local asymptotic" static observer.
[4] Mass-energy accretion rate from measurements of $M_{\rm BH}$; see Section 4.3.2.
[5] Rest-mass accretion rate from flux across horizon; see Section 4.3.3
[6] Rest-mass accretion rate from Bondi expressions; see Eq. (3.42).

Table 5.1: Accretion rates for different black hole masses embedded in our fiducial neutron star model (see Table 3.2). For all cases, the ratio between $M_{\rm BH}(0)$ and the neutron star rest mass M_0 is $M_{\rm BH}(0)/M_0 = 7.12 \times \tilde{\mathcal{M}}$. The accretion rates $\dot{M}_{\rm BH}$ and $\mathcal{F}(r_{\rm AH})$ are measured by a static observer at infinity. In order to compare these results with our rates as measured by a "local asymptotic" static observer in the neutron star core, $\dot{M}^\star_{\rm BH}$, we divide the $\dot{M}_{\rm BH}$ by the lapse $\alpha_\star$ of the local observer. In the last two columns, we observe that the numerically measured rest-mass flux $\mathcal{F}(r_{\rm AH})/\alpha_\star$ (see Section 4.3.3) agrees very well with the analytical value $\dot{M}^\star_{\rm BH}$ given by Bondi accretion (see Eq. 3.42). We also present these results in Fig. 1.1.

Although we must be careful in considering the comparison between the numerical results and analytical estimates, Fig. 5.2 shows reasonable agreement between them. Namely, we observe that the analytical estimate with stellar evolution improves the agreement with the numerical results. We convert our local analytical estimates to our global numerical results in our comparison using the value $\alpha_\star = 0.623$. However, we identified this value for smaller black hole masses embedded in our fiducial neutron star model, but as mentioned above, we are unable to determine this value at late times.

5.3 Accretion rates

We present our accretion results in Table 5.1 for our simulations of a large range of initial black hole masses, spanning seven orders of magnitude in $M_{\rm BH}/M$. We compute

the accretion rates for each black hole. For sufficiently large black holes as explained in Section 4.3.3, we compute the growth of the black hole $\dot{M}_{\rm BH}$, and for all black holes we compute the fluid flux $\dot{M}_{\rm BH} = \mathcal{F}(r_{\rm AH})$ as discussed in Section 4.3.2. To compute the rates measured by a local observer, we divide the "global" rates above by the lapse of a "local asymptotic observer" $\alpha_\star$ far inside the neutron star. We can also estimate these rates measured by a local observer from the Bondi expression for our fiducial neutron star model (3.42), and we list these results in the final column of Table 5.1. The entries in this Table are also shown in Fig. 1.1.

As mentioned above, we do not track the evolution to completion for the small black holes listed in Table 5.1 because it is not computationally feasible. Rather, our system evolves for a coordinate time of approximately $10^3 M_{\rm BH}$. By this time, the accretion rate has settled into equilibrium, so we can accurately measure the accretion rate.

Most importantly, our accretion rates agree excellently with each other as shown in Fig. 1.1. Namely, the flux of rest-mass across the horizon computed numerically agrees very well with the analytical accretion rates computed from relativistic Bondi accretion. We notice that the accretion rate computed from measuring the growth of the black hole horizon yields a slightly larger value. This may be due to the fact that this measure includes thermal energy in addition to rest-mass energy. This observation only holds for early times when the accretion process is described by Bondi accretion. Lastly, we note that our analytical estimate (4.21) with $\psi_c = 1.27$ for the initial black hole mass as given in Table 3.2 agrees excellently with our initial black hole mass $\tilde{M}_{\rm BH}(0)$.

Chapter 6

Conclusion

In this thesis, we study in detail the accretion onto an endoparasitic black hole residing at the center of a neutron star until the black hole completely consumes the neutron star. Various aspects of this problem have been studied previously (see, for example, Capela et al. (2013); East and Lehner (2019); Génolini et al. (2020)), and we expand on these treatments in multiple ways.

We determine the analytical Bondi accretion rate for stiff equations of state with $\Gamma > 5/3$ (see also Richards et al. (2021b); Baumgarte and Shapiro (2021)), allowing us to determine the constant of proportionality in the relation $\dot{M}_{\rm BH} \propto M_{\rm BH}^2$. From these results, we construct an approximate analytical model to track the evolution of an initially small black hole at the center of a neutron star until it completely consumes the neutron star.

We extend previous simulations from East and Lehner (2019) to significantly smaller mass ratios $M_{\rm BH}/M$ and perform numerical simulations of this accretion process for sufficiently long times so that the system reaches quasistationary accretion. We adopt spherical polar coordinates in our numerical code and use a logarithmic radial coordinate which allows us to resolve the drastically different length scales between the black hole mass $M_{\rm BH}$ and neutron star mass M.

In Fig. 1.1 we show that our numerical results and our analytical estimates agree remarkably well with each other over many orders of magnitude in $M_{\rm BH}/M$. Therefore, this allows us to determine the lifetime of a neutron star using these Bondi accretion rates for stiff equations of state. In particular, this lifetime is close to a nearly universal maximum lifetime that is roughly independent of the properties of the neutron star and its EOS, and depends on the initial black hole mass $M_{\rm BH}$ only, as reported in Baumgarte and Shapiro (2021).

Our results support arguments that use the existence of neutron star populations to constrain primordial black holes or dark matter particles that may form black holes at the center of neutron stars after they have been captured as possible sources of dark matter (see, e.g., Goldman and Nussinov (1989); de Lavallaz and Fairbairn (2010); Bramante and Linden (2014); Bramante and Elahi (2015); Capela et al. (2013); Bramante et al. (2018); East and Lehner (2019); Génolini et al. (2020)). We consider these constraints under the assumption that given certain cosmological densities and masses of these dark matter constituents, neutron star would capture these possible sources of dark matter and then be consumed by the black hole at times older than the ages of old neutron star populations. Primordial black holes in the mass range $10^{-15}M_\odot \lesssim M_{\rm BH} \lesssim 10^{-9}M_\odot$ (see, e.g., Capela et al. (2013); Kühnel and Freese (2017)) have been used in particular to constrain this argument.

Appendix A

Cubic equation solution for a_s^2

We follow Section 5.6 in Press et al. (2007) to compute the general solution of the cubic equation (2.18). We start by defining

$$Q \equiv \frac{A^2 - 3B}{9} = \frac{(3\Gamma - 2)^2}{81} \tag{A.1}$$

and

$$\begin{aligned} R &\equiv \frac{2A^3 - 9AB + 27C}{54} \\ &= \frac{1}{1458}\Big(54\,\Gamma^3 - 351\,\Gamma^2 + 558\,\Gamma + 486\,a_\infty^2(\Gamma - 1) - 243\,a_\infty^2 - 259\Big) \end{aligned} \tag{A.2}$$

and distinguish two different cases depending on whether the quantity

$$\begin{aligned} R^2 - Q^3 = \frac{(1 + a_\infty^2 - \Gamma)^2}{8748}\Big(243\left(a_\infty^4 - 2\,a_\infty^2(\Gamma - 1)\right) \\ - (5 - 3\Gamma)^2(12\Gamma - 11)\Big) \end{aligned} \tag{A.3}$$

is positive or negative. Solving for a root of (A.3) we see that we have $R^2 - Q^3 < 0$ whenever

$$a_\infty^2 < \Gamma - 1 + \frac{2\sqrt{3}}{27}\,(3\Gamma - 2)^{3/2}\,. \tag{A.4}$$

Evidently, this condition holds for all $a_\infty^2 \leq \Gamma - 1$, so that $R^2 - Q^3$ is negative for all physically viable solutions. The cubic equation (2.18) then has three roots that are given by,

$$\begin{aligned} x_1 &= -2\sqrt{Q}\cos\left(\frac{\theta}{3}\right) - \frac{A}{3} \\ x_2 &= -2\sqrt{Q}\cos\left(\frac{\theta + 2\pi}{3}\right) - \frac{A}{3} \\ x_3 &= -2\sqrt{Q}\cos\left(\frac{\theta - 2\pi}{3}\right) - \frac{A}{3}, \end{aligned} \tag{A.5}$$

where

$$\theta = \arccos\left(\frac{R}{Q^{3/2}}\right). \tag{A.6}$$

We note that the coefficients A, B, and C in Eq. (2.18) are all real and consequently R and Q are real as well, leading to three real roots. While there are three real solutions, only x_3 gives a physical solution as we are limited by Eq. (2.9) as shown in Figure (2.2).

Appendix B

Integration of Eq. (3.30)

In this appendix we outline how the differential equation (3.30) can be solved analytically.

We first separate variables to obtain

$$dT = -\frac{y^{7/2}dy}{(y_0 - y)^2} \tag{B.1}$$

and then integrate to find

$$T = -I, \tag{B.2}$$

where we have assumed that the initial time is chosen to vanish, $T_i = 0$, and where I is given by

$$I = \int \frac{y^{7/2}dy}{(y_0 - y)^2}. \tag{B.3}$$

This integral can now be integrated as follows.

Using partial fractions, we rewrite (B.3) as

$$\begin{aligned} I &= \int \frac{y^{7/2}dy}{(y_0 - y)^2} \\ &= \int y^{3/2}\frac{y^2 + (y_0 - y)^2 - (y_0 - y)^2}{(y_0 - y)^2}dy \\ &= \int y^{3/2}\frac{(y_0 - y)^2 + 2yy_0 - y_0^2}{(y_0 - y)^2}dy \\ &= \int y^{3/2}dy + 2y_0 \int y^{3/2}\frac{y - y_0/2}{(y_0 - y)^2}dy. \end{aligned} \tag{B.4}$$

Repeating the process twice more, we obtain

$$\begin{aligned} I &= \int y^{3/2}dy + 2y_0 \int y^{1/2}dy + 3y_0^2 \int y^{-1/2}dy \\ &\quad +4y_0^3 \int y^{-1/2}\frac{y - 3y_0/4}{(y_0 - y)^2}dy. \end{aligned} \tag{B.5}$$

We now split the last integral into two terms,

$$y_0^3 \int y^{-1/2} \frac{4y - 3y_0}{(y_0 - y)^2} dy \tag{B.6}$$
$$= 4y_0^3 \int \frac{y^{1/2}}{(y_0 - y)^2} dy - 3y_0^4 \int \frac{y^{-1/2}}{(y_0 - y)^2} dy$$

and use a hyperbolic trig substitution

$$y = y_0 \tanh^2 x \tag{B.7}$$

in both integrals, resulting in

$$4y_0^3 \int \frac{y^{1/2}}{(y_0 - y)^2} dy = 8y_0^{5/2} \int \sinh^2 x \, dx \tag{B.8}$$

and

$$3y_0^4 \int \frac{y^{-1/2}}{(y_0 - y)^2} dy = 6y_0^{5/2} \int \cosh^2 x \, dx. \tag{B.9}$$

Since

$$\int \sinh^2 x \, dx = \frac{1}{2} \sinh x \cosh x - \frac{x}{2} \tag{B.10}$$

and

$$\int \cosh^2 x \, dx = \frac{1}{2} \sinh x \cosh x + \frac{x}{2}, \tag{B.11}$$

as can be seen using integration by parts, we can combine results to find

$$y_0^3 \int y^{-1/2} \frac{4y - 3y_0}{(y_0 - y)^2} dy = y_0^{5/2} \left(\sinh x \cosh x - 7x \right). \tag{B.12}$$

We now rewrite $\sinh x \cosh x$ in terms of $\tanh x$ and insert the substitution (B.7) to obtain

$$y_0^3 \int y^{-1/2} \frac{4y - 3y_0}{(y_0 - y)^2} dy \tag{B.13}$$
$$= y_0^3 \frac{y^{1/2}}{y_0 - y} - 7y_0^{5/2} \tanh^{-1}(y/u_0)^{1/2}.$$

Finally we insert this expression into (B.5), and carry out the remaining integrations to find

$$\begin{aligned} I &= \frac{2}{5} y^{5/2} + \frac{4}{3} y_0 y^{3/2} + 6y_0^2 y^{1/2} \\ &\quad + y_0^3 \frac{y^{1/2}}{y_0 - y} - 7y_0^{5/2} \tanh^{-1}(y/y_0)^{1/2}. \end{aligned} \tag{B.14}$$

Combining the first four terms and using

$$\tanh^{-1}(x) = \frac{1}{2}\ln\left(\frac{1+x}{1-x}\right) \tag{B.15}$$

we can also write this result as

$$\begin{aligned} I &= y^{1/2}\frac{6y^3 + 14y_0y^2 + 70y_0^2y - 105y_0^3}{15(y-y_0)} \\ &\quad -\frac{7}{2}y_0^{5/2}\ln\left(\frac{y_0^{1/2}+y^{1/2}}{y_0^{1/2}-y^{1/2}}\right). \end{aligned} \tag{B.16}$$

Recall that $1-y = (M_{\rm BH} - M_{\rm BH}(0))/M(0)$ measures the fractional increase in the black hole mass (see Eqs. 3.27 and 3.28), and that $T = -I$ is proportional to the time as measured by a local asymptotic static observer (see Eq. 3.29).

Acknowledgments

I would like to acknowledge all of the support, help, and "reminders" from my honors advisor Professor Baumgarte. I would also like to acknowledge Professor Stuart L. Shapiro from the University of Illinois at Urbana-Champaign for his numerous contributions to this project. Lastly, I would like to thank Maria Perez Mendoza for many helpful conversations and support. This work was supported in parts by National Science Foundation (NSF) grants PHY-2010394 to Bowdoin College, and NSF grants PHY-1662211 and PHY-2006066 and National Aeronautics and Space Administration (NASA) grant 80NSSC17K0070 to the University of Illinois at Urbana-Champaign.

Bibliography

Alcubierre, M., B. Brügmann, P. Diener, M. Koppitz, D. Pollney, E. Seidel, and R. Takahashi (2003). Gauge conditions for long-term numerical black hole evolutions without excision. *Phys. Rev. D 67*(8), 084023.

Baumgarte, T. W., P. J. Montero, I. Cordero-Carrión, and E. Müller (2013). Numerical relativity in spherical polar coordinates: Evolution calculations with the BSSN formulation. *Phys. Rev. D 87*(4), 044026.

Baumgarte, T. W., P. J. Montero, and E. Müller (2015). Numerical relativity in spherical polar coordinates: Off-center simulations. *Phys. Rev. D 91*(6), 064035.

Baumgarte, T. W. and S. L. Shapiro (1999). Numerical integration of Einstein's field equations. *Phys. Rev. D 59*(2), 024007.

Baumgarte, T. W. and S. L. Shapiro (2010). *Numerical Relativity: Solving Einstein's Equations on the Computer*. Cambridge University Press.

Baumgarte, T. W. and S. L. Shapiro (2021, January). Neutron stars harboring a primordial black hole: Maximum survival time.

Begelman, M. C. (1978). Accretion of $V > 5/3$ Gas by a Schwarzschild Black Hole. *Astronomy and Astrophysics 70*, 583.

Bona, C., J. Massó, E. Seidel, and J. Stela (1995). New Formalism for Numerical Relativity. *Phys. Rev. Lett. 75*, 600–603.

Bonazzola, S., E. Gourgoulhon, P. Grandclément, and J. Novak (2004). Constrained scheme for the Einstein equations based on the Dirac gauge and spherical coordinates. *Phys. Rev. D 70*(10), 104007.

Bondi, H. (1952, January). On spherically symmetrical accretion. *Mon. Not. R. Astron. Soc. 112*, 195.

Bramante, J. and F. Elahi (2015). Higgs portals to pulsar collapse. *Phys. Rev. D 91*(11), 115001.

Bramante, J. and T. Linden (2014). Detecting Dark Matter with Imploding Pulsars in the Galactic Center. *Phys. Rev. Lett. 113*(19), 191301.

Bramante, J., T. Linden, and Y.-D. Tsai (2018). Searching for dark matter with neutron star mergers and quiet kilonovae. *Phys. Rev. D 97*(5), 055016.

Brandt, S. and B. Brügmann (1997). A Simple Construction of Initial Data for Multiple Black Holes. *Phys. Rev. Lett. 78*(19), 3606–3609.

Brown, J. D. (2009). Covariant formulations of Baumgarte, Shapiro, Shibata, and Nakamura and the standard gauge. *Phys. Rev. D 79*(10), 104029.

Capela, F., M. Pshirkov, and P. Tinyakov (2013). Constraints on primordial black holes as dark matter candidates from capture by neutron stars. *Phys. Rev. D 87*(12), 123524.

Carr, B. J. and S. W. Hawking (1974). Black holes in the early Universe. *Mon. Not. R. Astron. Soc. 168*, 399–416.

Chaverra, E., P. Mach, and O. Sarbach (2016). Michel accretion of a polytropic fluid with adiabatic index \5/3: global flows versus homoclinic orbits. *Classical and Quantum Gravity 33*(10), 105016.

de Lavallaz, A. and M. Fairbairn (2010). Neutron stars as dark matter probes. *Phys. Rev. D 81*(12), 123521.

East, W. E. and L. Lehner (2019). Fate of a neutron star with an endoparasitic black hole and implications for dark matter. *Phys. Rev. D 100*(12), 124026.

Einfeldt, B. (1988). On godunov methods for gas dynamics. *SIAM J. Numer. Anal. 25*, 294.

Farris, B. D., Y. T. Liu, and S. L. Shapiro (2010). Binary black hole mergers in gaseous environments: "Binary Bondi" and "binary Bondi-Hoyle-Lyttleton" accretion. *Phys. Rev. D 81*(8), 084008.

Fuller, G. M., A. Kusenko, and V. Takhistov (2017). Primordial Black Holes and r -Process Nucleosynthesis. *Phys. Rev. Lett. 119*(6), 061101.

Génolini, Y., P. D. Serpico, and P. Tinyakov (2020). Revisiting primordial black hole capture into neutron stars. *Phys. Rev. D 102*(8), 083004.

Goldman, I. and S. Nussinov (1989). Weakly interacting massive particles and neutron stars. *Phys. Rev. D 40*(10), 3221–3230.

Gourgoulhon, E. (2012). *3+1 Formalism in General Relativity*. Springer, Berlin.

Harten, A., P. D. Lax, and v. B. Leer (1983). On upstream differencing and Godunov type methods for hyperbolic conservation laws. *SIAM Rev. 25*, 35–61.

Hawking, S. (1971). Gravitationally collapsed objects of very low mass. *Mon. Not. R. Astron. Soc. 152*, 75.

Kouvaris, C. and P. Tinyakov (2014). Growth of black holes in the interior of rotating neutron stars. *Phys. Rev. D 90*(4), 043512.

Kühnel, F. and K. Freese (2017). Constraints on primordial black holes with extended mass functions. *Phys. Rev. D 95*(8), 083508.

Markovic, D. (1995). Evolution of a primordial black hole inside a rotating solar-type star. *Mon. Not. R. Astron. Soc. 277*(1), 25–35.

Mewes, V., Y. Zlochower, M. Campanelli, T. W. Baumgarte, Z. B. Etienne, F. G. L. Armengol, and F. Cipolletta (2020). Numerical relativity in spherical coordinates: A new dynamical spacetime and general relativistic MHD evolution framework for the Einstein Toolkit. *Phys. Rev. D 101*(10), 104007.

Mewes, V., Y. Zlochower, M. Campanelli, I. Ruchlin, Z. B. Etienne, and T. W. Baumgarte (2018). Numerical relativity in spherical coordinates with the Einstein Toolkit. *Phys. Rev. D 97*(8), 084059.

Michel, F. C. (1972, January). Accretion of Matter by Condensed Objects. *Astrophys. Space Sci. 15*(1), 153–160.

Miller, A. J. and T. W. Baumgarte (2017). Bondi accretion in trumpet geometries. *Classical and Quantum Gravity 34*(3), 035007.

Montero, P. J., T. W. Baumgarte, and E. Müller (2014). General relativistic hydrodynamics in curvilinear coordinates. *Phys. Rev. D 89*(8), 084043.

Nakamura, T., K. Oohara, and Y. Kojima (1987). General Relativistic Collapse to Black Holes and Gravitational Waves from Black Holes. *Progress of Theoretical Physics Supplement 90*, 1–218.

Oppenheimer, J. R. and G. M. Volkoff (1939). On Massive Neutron Cores. *Physical Review 55*(4), 374–381.

Press, W. H., S. A. Teukolsky, W. T. Vetterling, and B. P. Flannery (2007). *Numerical Recipes: The Art of Scientific Computing*. Cambridge University Press.

Richards, C. B., T. W. Baumgarte, and S. L. Shapiro (2021a, February). Accretion onto a small black hole at the center of a neutron star. *arXiv e-prints*, arXiv:2102.09574.

Richards, C. B., T. W. Baumgarte, and S. L. Shapiro (2021b, April). Relativistic Bondi accretion for stiff equations of state. *Mon. Not. R. Astron. Soc. 502*(2), 3003–3011.

Ruchlin, I., Z. B. Etienne, and T. W. Baumgarte (2018). SENR /NRPy + : Numerical relativity in singular curvilinear coordinate systems. *Phys. Rev. D 97*(6), 064036.

Shapiro, S. L. and S. A. Teukolsky (2004). *Black Holes, White Dwarfs, and Neutron Stars: The Physics of Compact Objects*. Wiley-VCH.

Shibata, M. and T. Nakamura (1995). Evolution of three-dimensional gravitational waves: Harmonic slicing case. *Phys. Rev. D 52*(10), 5428–5444.

Shibata, M., K. Uryū, and J. L. Friedman (2004). Deriving formulations for numerical computation of binary neutron stars in quasicircular orbits. *Phys. Rev. D 70*(4), 044044.

Takhistov, V., G. M. Fuller, and A. Kusenko (2020). A Test for the Origin of Solar Mass Black Holes.

Thierfelder, M., S. Bernuzzi, and B. Brügmann (2011). Numerical relativity simulations of binary neutron stars. *Phys. Rev. D 84*(4), 044012.

Tolman, R. C. (1939). Static Solutions of Einstein's Field Equations for Spheres of Fluid. *Physical Review 55*(4), 364–373.

van Leer, B. (1977). Towards the ultimate conservative difference scheme: IV. A new approach to numerical convection. *Journal of Computational Physics 23*, 276–299.